

1 **CryoEM structure of the outer membrane secretin channel pIV from the f1 filamentous**
2 **bacteriophage**

3

4 Rebecca Conners^{1,2}, Mathew McLaren^{1,2}, Urszula Łapińska^{1,2}, Kelly Sanders^{1,2}, M. Rhia L.
5 Stone³, Mark A. T. Blaskovich³, Stefano Pagliara^{1,2}, Bertram Daum^{1,2}, Jasna Rakonjac⁴ &
6 Vicki A. M. Gold^{1,2*}

7

8 ¹ Living Systems Institute, University of Exeter, Stocker Road, Exeter EX4 4QD, UK

9 ² College of Life and Environmental Sciences, Geoffrey Pope, University of Exeter, Stocker
10 Road, Exeter EX4 4QD, UK

11 ³Centre for Superbug Solutions, Institute for Molecular Bioscience, The University of
12 Queensland, Brisbane, Queensland 4072, Australia

13 ⁴School of Fundamental Sciences, Massey University, Palmerston North, New Zealand

14 *Corresponding author: v.a.m.gold@exeter.ac.uk

15

16 **Abstract**

17 The Ff family of filamentous bacteriophages infect gram-negative bacteria, but do not cause
18 lysis of their host cell. Instead, new virions are extruded via the phage-encoded pIV protein,
19 which has homology with bacterial secretins. Here, we have determined the structure of pIV
20 from the f1 filamentous bacteriophage at 2.7 Å resolution by cryo-electron microscopy, the
21 first near-atomic structure of a phage secretin. Fifteen f1 pIV monomers assemble to form a
22 gated channel in the bacterial outer membrane, with associated soluble domains projecting
23 into the periplasm. We model channel opening and propose a mechanism for phage-mediated
24 gate movement. By single-cell microfluidics experiments, we demonstrate the potential for
25 secretins such as pIV to be used as adjuvants to increase the uptake and efficacy of antibiotics

26 in bacteria. Finally, we compare the f1 pIV structure to its homologues to reveal similarities
27 and differences between phage and bacterial secretins.

28

29 **Keywords**

30 Filamentous bacteriophage, secretin, pIV, cryo-electron microscopy, single-cell
31 microfluidics, antimicrobial resistance

32

33 **Introduction**

34 The Ff family of filamentous bacteriophages includes f1, fd and M13, and is one of the
35 simplest biological systems known¹. Filamentous phages such as Ff have many uses in
36 biotechnology and nanotechnology²; examples include as a cloning vector, and in phage
37 display for screening protein-ligand and protein-protein interactions. Ff is also increasingly
38 employed in nanotechnology, being engineered to adopt a variety of different forms such as
39 nano-wires, nanorings and branched structures^{3,4}. With the recent, and much publicised,
40 global antimicrobial resistance crisis^{5,6}, there has been a renewed campaign in exploring the
41 use of phages and their proteins to target pathogenic bacteria^{7,8}. Understanding the structural
42 and functional details of phage lifecycles is thus of broad interest for both fundamental and
43 applied biological science research.

44

45 Phages f1, fd and M13 share 98.5% sequence identity and infect the gram-negative bacterium
46 *Escherichia coli*. The primary binding receptor is the F-pilus - a long filamentous appendage
47 assembled on the bacterial cell surface. Phage virions are 1 µm long and 6-7 nm wide, with a
48 circular single-stranded DNA genome encoding for 11 viral proteins. The viral genome is
49 encapsulated within several thousand copies of the major viral coat protein pVIII and is
50 capped by protein complexes consisting of pIII/pVI and pVII/pIX at either end⁹.

51 Phages bind to the F-pilus via the pIII/pVI cap, which is followed by pilus retraction and
52 binding of phage to the TolQRA complex in the host cell inner membrane¹⁰. The phage
53 genome is released into the bacterial cytoplasm, DNA is replicated and phage proteins are
54 expressed¹¹. New virions are assembled and released from the cell via a complex of three
55 phage-encoded proteins, pI, pXI and pIV. pI (an ATPase) and pXI span the inner membrane
56 with pIV located in the outer membrane^{12,13}.

57

58 pIV is a secretin family protein, with sequence similarity to bacterial secretins at the core of
59 the Type IV pilus assembly machinery and the Type II and Type III secretion systems¹⁴. A
60 number of high-resolution structures of bacterial secretins have been determined¹⁵⁻¹⁸, which
61 have allowed detailed comparisons to be made^{19,20}. All secretins are multimeric channel
62 proteins, ranging in molecular weight from 670 kDa to >1 MD. Reports of stoichiometry
63 range between twelve and fifteen monomers per complex, divided into a number of different
64 domains. The C-terminal domain integrates into the bacterial outer membrane and forms a
65 double-walled β -barrel with a central gate forming a stricture at the centre²¹. Varying
66 numbers of soluble N-domains connect to the β -barrel and project into the periplasm. The N-
67 domains are often poorly ordered in cryo-electron microscopy (cryoEM) structures,
68 presumably due to their flexibility. Type II secretins can also differ at the externally-exposed
69 side of the β -barrel, with *Vibrio*-type complexes possessing a cap gate and *Klebsiella*-type
70 lacking this feature¹⁹.

71

72 A cryoEM structure of the f1 pIV (f1pIV) protein determined at 22 Å resolution²² showed a
73 barrel-like complex with a large pore running through the centre containing a pore-gate. We
74 present here the cryoEM structure of f1pIV to 2.7 Å resolution, the first near-atomic
75 resolution structure of a phage secretin protein. By computational modelling and correlation

76 of our structure to a large library of phenotypic mutants, we propose a mechanism for channel
77 opening and interaction of f1pIV with phage. We also employ a mutant of f1pIV that
78 produces a “leaky” *E. coli* phenotype and demonstrate by single-cell microfluidics that the
79 macrolide antibiotic roxithromycin is taken up efficiently by the f1pIV-expressing bacteria.
80 The f1pIV atomic structure is used to interpret these findings, which have important
81 translational implications for the use of secretins as therapeutic adjuvants to increase
82 antibiotic delivery to bacteria. Finally, we reveal the common structural motifs shared by
83 f1pIV and bacterial secretins, and differences in their electrostatic surface charges and
84 modular architecture.

85

86 **Results**

87 **Structure of the f1pIV secretin**

88 The 670 kDa f1pIV secretin channel was expressed recombinantly in *E. coli* and purified in
89 the presence of CHAPS detergent by Ni²⁺ affinity and size exclusion chromatography. Pure
90 protein was identified by SDS-PAGE, Western blot and mass spectrometry analysis
91 (Supplementary Fig. 1). CryoEM data were collected and processed in Relion 3.1²³
92 (Supplementary Table 1). Averaging the protein particles together in 2D showed that f1pIV
93 particles are composed of fifteen identical copies of the monomer (Fig. 1a); no variation in
94 symmetry was observed. 3D reconstruction produced a 2.7 Å map with C15 symmetry
95 applied (Fig. 1b and Supplementary Fig. 2).

96

97 The N-terminal part of f1pIV is comprised of two periplasmic N domains: the far N-terminal
98 N0 domain (residues 1-88) and the N3 domain (108-172), which are joined together with a
99 19-residue linker (89-107) (Fig. 2a). The N3 domain links to the C-terminal secretin domain
100 (175-405) via a two amino acid linker (173-174) (Fig. 2a). The quality of our map allowed

101 the N3 and secretin domains to be unambiguously modelled into the density (Fig. 1c, 2b, c),
102 with clear side chain densities visible in most areas (Fig. 2d). The fifteen monomers pack
103 against each other to form the secretin channel, with each monomer contributing a four-
104 stranded β -sheet to the multimer, culminating in a large β -barrel composed of 60 β -strands
105 (Fig. 2b, c). The β -sheets lie at an angle of 41° relative to the central axis of the pore. Within
106 the β -barrel is a smaller inner barrel comprised of four β -strands from each f1pIV monomer
107 (Fig. 2c, e-g). The inner β -barrel is angled parallel to the pore axis and provides a scaffold for
108 two extended loops that reach into the centre of the pore, known as Gate 1 and Gate 2²⁴ (Fig.
109 2c, g). The interface between the outer and inner β -barrels is composed mostly of
110 hydrophobic residues, and strengthened further with a salt bridge between Glu 185 and Arg
111 337 (both residues are highly conserved amongst homologues) (Fig. 2e, Supplementary Fig. 3
112 and 4). Extensive hydrogen bonds are formed within the inner and outer β -barrels; within
113 each individual monomer, and also between each monomer and its immediate neighbours
114 (Fig. 2f). In the outer β -barrel, monomer 1 forms 15 intra-subunit hydrogen bonds, and 12
115 inter-subunit hydrogen bonds (6 with each neighbouring monomer). In the inner β -barrel,
116 monomer 1 forms 26 intra-subunit hydrogen bonds and 14 inter-subunit ones (7 with each
117 neighbouring monomer). The interface between neighbouring N3 domains is mostly
118 hydrophobic, and no hydrogen bond interactions are observed between them in our structure.
119 For reasons of flexibility (Supplementary Fig. 2), the extracellular part of the β -barrel was
120 missing interpretable density (36 amino acid residues, positions 199-234) as well as part of
121 the Gate 1 loop (residues 275-289) at the very centre of the pore.

122

123 The f1pIV secretin measures 96 \AA from the extracellular face of the β -barrel to the N-
124 terminus of the N3 domain, and 112 \AA across at its widest point (the extracellular part of the
125 β -barrel. The diameter across the inner β -barrel is 90 \AA . The pore width is constricted further

126 in two areas; at the central gate (40 Å) and at the N3 domains (74 Å). There are however
127 disordered loops in both the N3 domain and Gate 1, both pointing into the centre of the pore,
128 so these distances could be smaller.

129
130 The globular N3 domain consists of 65 residues which fold to form a three-stranded β -sheet
131 packed against two α -helices, joined by the short two amino acid linker to the β -barrel (Fig.
132 2a, c, g). The far N-terminal N0 domain and its associated 19 residue linker region (residues
133 1-107, Fig. 2a) could not be observed in our structure. In the 2D classes, a hazy area could be
134 seen in the expected region, suggesting that N0 could be present but extremely flexible (Fig.
135 1a, red arrow). Tryptic digest mass spectrometry was used to confirm that all of the regions
136 for which we either did not see density, or could not interpret the density, were physically
137 present (Fig. 2a).

138
139 To provide insight into the structure of the N0 domain, we employed three complementary
140 methods. We performed a Blast search of f1pIV N0 plus the associated linker region
141 (residues 1-107) against all structures in the Protein Data Bank. This resulted in a single hit
142 for the PulD secretin from *Klebsiella pneumoniae* (6HCG) with 33% sequence identity over
143 63 residues. We used this structure to produce a homology model of the f1pIV N0 domain in
144 Swiss-Model²⁵. The same f1pIV N0-linker domain sequence was also submitted to the I-
145 TASSER²⁶ and Robetta structural prediction servers²⁷. The resulting models from all methods
146 were compared and seen to be in agreement for the folded domain (residues 2-71)
147 (Supplementary Fig. 5). The N0 domain is thus most likely formed by two α -helices, flanked
148 by a two-stranded β -sheet on one side and a three-stranded β -sheet on the other. We used the
149 structure from I-TASSER to generate a composite model with our f1pIV structure (Fig. 2g).
150 The three N0 models diverge at residues 72-107, which is in agreement with this region being

151 a flexible linker (Figure 2a, Supplementary Fig. 5). The linker region has been modelled in a
152 fully extended conformation and the position of the N0 domain obtained by overlaying the
153 f1pIV structure with that of the *Klebsiella* PulD secretin (6HCG²⁸, Supplementary Fig. 5); the
154 distance between N0 and N3 could be closer if the linker takes on a more compact structure.
155 The entire length of f1pIV (from the extracellular face of the β -barrel to the N-terminal
156 periplasmic domain of N0) in our composite model is 220 Å. This agrees well with the
157 distance needed for f1pIV to cross the *E. coli* periplasm (with a width of 210 Å)²⁹ and reach
158 the pI/pXI proteins in the inner membrane.

159

160 **Membrane integration of f1pIV**

161 An additional band of density was observed in our EM map which was unaccounted for,
162 lying in approximately the centre of the surface of the β -barrel (Fig. 3a). This formed a ring
163 around the outside of the secretin domain, reminiscent of detergent belts typically seen in
164 cryoEM structures of membrane proteins³⁰. We modelled the detergent CHAPS, used during
165 purification, into this density. Two molecules of CHAPS were observed to bind to each f1pIV
166 monomer, forming a circle of detergent around the barrel (Fig. 3b). The detergent molecules
167 were bound to a ring of aromatic residues (Phe 184, Tyr 359 and Tyr 394), forming an
168 aromatic girdle. An additional aromatic girdle was observed nearer the extracellular region of
169 the β -barrel formed by Phe 194 and Phe 196. Such clusters of aromatic residues are often
170 observed at the lipid-water interface in membrane-spanning β -barrels of gram-negative
171 bacteria, and allow for protein positioning in the membrane³¹. Colouring the surface of f1pIV
172 by hydrophobicity confirms that the two aromatic girdles lie within the two main regions of
173 high hydrophobicity on the protein surface (Fig. 3c).

174

175 **The Gate region**

176 The inner β -barrel, Gate 1 (G267-G297) and Gate 2 loops (D321-Q336) form the full gate
177 region that projects into the pore. The Gate 1 loops extend to the centre, presumably sealing
178 the channel. Sequence alignments show high sequence conservation for Gate 1 amongst
179 secretin homologues, while Gate 2 is less well conserved (Supplementary Fig. 3). In both
180 cases, the areas of highest sequence conservation are found where the gates join the inner β -
181 barrel, with the more variable regions lying in the loop regions which face the centre of the
182 pore. There are two highly conserved glycine residues found at the boundary of Gate 1,
183 which are believed to form a hinge for gate opening³² (Fig. 4a). An extensive hydrogen
184 bonding network was observed within the gate region (Fig. 4a). Hydrogen bonds are formed
185 within each gate (5 intra-gate bonds in Gate 1, and 2 intra-gate bonds in Gate 2), tethering
186 each loop together tightly. As seen in all other secretin structures to date, the Gate 1 loop has
187 an unusual twisted conformation. Inter-gate hydrogen bonds are formed between
188 neighbouring subunits in the multimer, with Gate 1 from one chain forming two hydrogen
189 bonds with Gate 2 from the neighbouring chain (Fig. 4a, b). A highly conserved Arg 293 in
190 Gate 1 is observed with clear density in a buried position. It forms hydrogen bonds with the
191 side chain of a conserved Asn 269 within the same gate, and with the backbone carbonyl
192 oxygen of Val 332 from Gate 2 of the neighbouring subunit (Fig. 4b, Supplementary Fig. 3),
193 adding further inter-subunit stability to the gate region.

194

195 **Opening the f1pIV channel**

196 The f1pIV pore must undergo significant structural rearrangements to allow phage to egress.
197 To provide insight into the mechanism of channel opening, we compared our f1pIV structure
198 to existing closed and open gate structures of a homologous protein: the Type III secretin
199 InvG from *Salmonella typhimurium* (6PEE and 6Q15)³³. Structural alignment of the two
200 InvG structures highlights the main differences between the open and closed states

201 (Supplementary Fig. 6). The core of the secretin domain and the conformation of the loops
202 remain similar; differences are seen in the position of the gate loops relative to the barrel, the
203 β -lip and an extended loop in the N3 domain. Both gate loops move to pack against the outer
204 β -barrel in the open form. The Gate 1 loop moves with a hinge-like motion, while the Gate 2
205 loop twists. The β -lip at the extracellular edge of the β -barrel also moves away from the
206 centre of the pore in the open structure, and there is movement of an extended loop (not
207 present in f1pIV) in the N3 domain. Our closed f1pIV structure aligns well to the InvG closed
208 state, with a Root Mean Square Deviation (RMSD) of 1.051 Å (Supplementary Fig. 6). The
209 f1pIV closed gate loops were thus modelled into the open form based on their position in
210 InvG (Supplementary Fig. 6 and Fig. 4c).

211
212 This model reveals how Gate 1 would likely pivot upwards and outwards on the highly
213 conserved hinge residues Gly 267 and Gly 297, located at the top of the inner β -barrel (Fig.
214 4a, c, d, Supplementary Fig. 3). The twisting motion in Gate 2 could occur around the
215 conserved Asp 321 and Asn 335 (Fig. 4d, Supplementary Fig. 3). These movements would
216 move both gate loops closer to the outer β -barrel and thus result in an opening of the pore
217 from the \sim 40 Å measured in our closed structure to 65 Å (Fig. 4e). This would enable the
218 virus particle (60 Å in diameter) to pass through the pore (Fig. 4f). A fibre diffraction
219 structure of an fd phage (2C0W) at 3.2 Å resolution³⁴ was coloured by electrostatic potential
220 (Fig. 4g) and shows a clear negative charge on its outer surface. In contrast, the electrostatic
221 surface potential within the f1pIV pore is more varied. In closed and open states, there is a
222 band of positive charge in the area closest to the extracellular side, followed by a band of
223 negative charge near the gate region. In the open state, the aperture revealed by gate opening
224 is mostly positively charged (Fig. 4g).

225

226 **Mapping mutations to f1pIV that cause a “leaky” *E. coli* phenotype**

227 Wild type *E. coli* cells (strain K12) cannot transport the bile salt deoxycholate across their
228 outer membranes, and those which are deficient in the LamB maltoporin cannot transport
229 large maltooligosaccharide sugars. Previous studies^{24,35,36} have revealed a number of
230 mutations in the f1pIV protein that render the pore leaky to these substrates. Leaky mutations
231 discovered by random mutagenesis (Supplementary Table 2)²⁴ have now been mapped on to
232 the f1pIV structure (Fig. 5a, b). The overwhelming majority (90%) were found to lie in the
233 gate region (the Gate 1 and Gate 2 loops or inner β -barrel). Three mutations (A121V, D123Y,
234 G147V) conferring leakiness to deoxycholate and maltopentaose were identified in the N3
235 domain, all at the interface closest to the inner β -barrel; one mutation (I183V) was observed
236 in the outer β -barrel (Fig. 5a). The authors also tested susceptibility of *E. coli* expressing
237 different f1pIV mutants to the antibiotics vancomycin and bacitracin (which are too large to
238 cross the bacterial outer membrane). By mapping these to our f1pIV structure, we can show
239 that all mutants which conferred antibiotic susceptibility were located in the gate region (4
240 with sensitivity to vancomycin alone, 12 with sensitivity to both vancomycin and bacitracin)
241 (Fig. 5b).

242

243 We used the map of f1pIV mutants to understand more about the delicate balance of
244 interactions in the gates (Supplementary Table 2). The conserved Gate 1 hinges (Gly 267 and
245 Gly 297) pack closely together within the inner β -barrel (Fig. 4d). Changing Gly 267 or Gly
246 297 to any other sidechain in the model causes steric clashes. Hinge mutations would thus
247 disrupt the packing in the region, interfere with hinge motion and prevent proper gate closure.
248 Asn 269, Arg 293 and Asn 295 in Gate 1 take part in a tight hydrogen bonding network in the
249 closed structure, with the Arg 293 sidechain being buried (Fig 4b; Supplementary Fig. 7).

250 Disrupting the hydrogen bonding network within the Gate 1 loop and between two
251 neighbouring gates would thus lead to a more dynamic and open gate structure.

252

253 **Antibiotic uptake through an f1pIV leaky mutant**

254 The antibiotic vancomycin is hydrophilic and bacitracin is amphipathic; both are sufficiently
255 small to pass through the open f1pIV pore (Supplementary Fig. 8). *E. coli* expressing the
256 previously characterised f1pIV mutant S324G are sensitive to both antibiotics, and still
257 functional for phage assembly^{24,37}. Ser 324 is located in Gate 2, where mutation to a glycine
258 will destroy the hydrogen bond made between the Ser 324 sidechain and the backbone
259 nitrogen of Ser 326 (Fig. 5c). Mutation to a glycine could also change the position of the
260 peptide backbone, potentially altering the hydrogen bonds that are currently made between
261 the Ser 324 carbonyl oxygen and the sidechain of Gln 328 from the neighbouring monomer,
262 and those made between the backbone nitrogen of Ser 324 and the carbonyl oxygen of Ile 333
263 (Fig. 5c). The combined effect of these mutations likely results in increased mobilisation of
264 the gate.

265

266 Building on this knowledge, here we aimed to understand whether the uptake and efficacy of
267 hydrophobic antibiotics could be improved by expressing leaky f1pIV in *E. coli*.

268 Hydrophobic macrolides are often used as first-line antibiotics, however, they are used
269 typically to treat infections caused by gram-positive but not most gram-negative bacteria due
270 to slow uptake across the outer membrane³⁸. The macrolide antibiotic roxithromycin is
271 widely clinically employed³⁹, and our modelled open gate structure reveals that it is
272 sufficiently small to pass through the open f1pIV channel unhindered (Supplementary Fig. 8).
273 Using single-cell analysis with the microfluidic mother machine and time-lapse
274 microscopy^{40,41}, bacteria were injected into channels and the accumulation of fluorescent

275 antibiotics measured⁴². Specifically, we employed a recently introduced fluorescent
276 derivative of roxithromycin (roxithromycin linked to nitrobenzoxadiazole -roxithromycin-
277 NBD), which largely maintains the antibiotic potency of the parental drug³⁸. *E. coli* cells
278 expressing f1pIV^{S324G} became distinguishable from the background within 700 s after adding
279 roxithromycin-NBD to our microfluidic device (Fig. 5d), suggesting rapid intracellular
280 accumulation. In contrast, *E. coli* cells expressing wild type f1pIV (f1pIV^{WT}) remained
281 largely indistinguishable from the background during exposure to roxithromycin-NBD (Fig.
282 5d), suggesting negligible accumulation. In agreement with these data, when we measured
283 the minimum inhibitory concentration (MIC) for roxithromycin, there was a one-notch shift
284 in the MIC of roxithromycin against the mutant compared to the wild-type (64 and 96 µg/ml,
285 respectively).

286

287 **Structural comparison of f1pIV with other secretins**

288 As our structure is the first of a viral secretin at near-atomic level, we compared f1pIV to
289 different classes of bacterial secretins^{32,33,43} (Fig. 6a, b, c, Supplementary Fig. 9). All
290 secretins share the same overall architecture of the double-walled β-barrel and the first and
291 last periplasmic domains (N0 and N3), but differ in the number of additional N domains
292 (reviewed by Filloux and Voulhoux¹⁹). The Gate 1 and Gate 2 loops are all in similar
293 conformations, pointing into the centre of the pore from the inner β-barrel. The N3 domains
294 are broadly similar, with the one notable difference being an extended loop region in the
295 Type III InvG secretin which extends up towards the central gate area (Fig. 6c;
296 Supplementary Fig. 9). In general, there is increasing disorder within domains closest to the
297 N-terminus, and many structures have no clear density for their N0 domains.

298

299 Differences between secretins are seen on the extracellular face of the β -barrel with the
300 Klebsiella-like group of Type II secretins having a cap gate which forms a much narrower
301 opening when compared to the other open-edged β -barrels. From sequence analysis
302 (Supplementary Fig. 4), we believe f1pIV will not have a cap structure at the extracellular
303 side of the β -barrel, but we could not see this region in our cryoEM map, likely for reasons of
304 flexibility (Supplementary Fig. 2). We are missing density for 36 residues, which is the
305 typical size of the β -lip domain in phage secretins (Supplementary Fig. 4). In contrast, the
306 bacterial Type II secretins typically have 51-60 residues in the β -lip region, while those with
307 a cap gate have around 80 residues here. Phage secretins are therefore expected to have a
308 more compact β -lip structure than their bacterial counterparts.

309
310 At the far C terminus of the protein, the Type II and Type III secretins have a helical domain
311 (the S-domain) that packs against the outside wall of the outer β -barrel. The S-domain binds
312 pilotin molecules, which are essential for the assembly and/or localisation of secretins to the
313 outer membrane. f1pIV and the Type IV pilus secretins do not have an S-domain, with their
314 respective C-termini being located at the periplasmic side of the outer β -barrel (Fig. 6c).
315 Interestingly, the Type IV pilus secretins bind to their pilotin partner via a hydrophobic girdle
316 around the β -barrel, in a similar place to the central hydrophobic girdle that we have observed
317 in f1pIV (Supplementary Fig.10).

318
319 We used the ConSurf server⁴⁴ to perform a sequence alignment of f1pIV homologues, map
320 them to the f1pIV structure and colour them by the degree of sequence conservation (Fig.
321 6d). The area of greatest conservation lies within the inner β -barrel and the region of outer β -
322 barrel that packs against it, demonstrating the importance of this region for protein stability
323 and/or function. The N3 domain is more variable, likely as a result of evolution to suit the

324 function of the individual system. We also compared the electrostatic surface potential
325 between the different classes of secretins (Fig. 6b and Supplementary Fig. 9). The outside
326 surfaces have a mixture of positively and negatively charged areas, with some very clear
327 bands of hydrophobicity, as expected for outer membrane proteins. The surface charge inside
328 the secretins is quite varied; differences presumably arose to accommodate the particular
329 shapes and electrostatic charges of substrate that each secretin transports.

330

331 **Discussion**

332 f1pIV is the first near-atomic resolution example of a phage secretin. The protein has a
333 similar overall architecture to bacterial secretins, but differs in its electrostatic surface
334 potential inside the pore and in the number of N domains. f1pIV is relatively compact, with
335 no cap gate, no C-terminal S-domain, and one N3 and one N0 domain; an arrangement which
336 could have arisen to save valuable space in the limited capacity of the phage genome.

337

338 The phenotypes of many previously characterised mutants can be rationalised with our
339 structure. f1pIV shows extensive hydrogen bonding within the outer and inner β -barrel
340 domains, as well as hydrophobic interactions and a salt bridge between the inner and outer
341 walls. Mutation of two conserved hydrophobic residues at the interface to glycines (I312G
342 and I314G) prevents multimer formation²⁴. In addition, inclusion of a His-tag on the external
343 loop between the inner and outer β -barrels has a destabilising effect, but this can be rescued
344 by introducing a hydrophobic mutation (S318I)⁴⁵, which lines the interface. The conserved
345 hydrophobic residues between inner and outer β -barrels are clearly important for folding and
346 stability, and highlight the importance of the unusual double-walled architecture.

347

348 In order for the phage to pass through f1pIV, the central gate must open. The conserved
349 architecture of the secretin family can be used to predict the mechanism (Fig. 7). The N-
350 terminal periplasmic N0 domain is extremely dynamic, likely due to the absence of the
351 phage-encoded pI/pXI inner membrane interaction partners. This flexibility may allow f1pIV
352 to sample a wider amount of periplasmic space than a rigid structure, allowing the N0
353 domains to locate and bind to the inner membrane assembly proteins and egressing phage.
354 pI/pXI interaction with f1pIV is required for phage assembly⁴⁶, therefore this suggests that
355 gate opening may be triggered by interaction of the N0 domain of f1pIV with the pI/pXI
356 inner membrane components. It is tempting to speculate that this could result in energy
357 transfer from the pI ATPase to help drive phage egress¹³. The egressing phage will
358 subsequently encounter the N3 domain; the involvement of N3 in channel opening has also
359 been predicted for Type II and Type III secretins^{16,32,33,47}. Introducing mutations into the N3
360 domain of f1pIV causes partial gate opening²⁴, highlighting its role in transducing
361 information from the periplasmic N domains into the β -barrel.

362
363 Our model of the open state of f1pIV highlights how the central gate loops will likely move
364 to allow phage to egress via the two conserved glycine hinge residues on the extracellular
365 side of the inner β -barrel³². A 10 residue in-frame deletion in Gate 2 results in leaky
366 multimers that are non-functional in phage assembly and egress²⁴, suggesting that passage of
367 phage through f1pIV is not a passive process. It is plausible that interaction of the f1 cap
368 proteins pVII/pIX with the f1pIV gate will be required to fully open the pore, assisted by the
369 force of the assembling f1 phage. The hydrogen bonding within Gate 1 and Gate 2 means that
370 the loops do not alter their conformation significantly, rather both loops are pivoted around
371 their hinges. The hydrogen bonds between neighbouring monomers means that all gates
372 would move synchronously. The surface of the phage has a high negative charge, while the

373 inner pore surface of the secretin is positively charged in the periplasmic chamber. This
374 opposing charge would presumably help to prevent friction and may drive the continued
375 movement of phage through the pore. *E. coli* expressing the leaky mutant f1pIV^{E292K}
376 exhibited the highest sensitivity to antibiotics and approximately a 10-fold decrease in phage
377 assembly relative to wild-type²⁴. The negatively charged sidechain of Glu 292 points into the
378 lower cavity of the pore (Supplementary Fig. 7). Replacing this with a positively charged
379 lysine residue would alter the electrostatic potential in this area, thus interfering with phage
380 interaction and egress.

381
382 f1pIV shows most sequence homology to GspD from *Klebsiella pneumoniae* (Supplementary
383 Fig. 11), and thus it is plausible that the ancestral f1 phage captured a Type II secretin which
384 subsequently evolved to meet the needs of phage assembly and egress. Indeed, a number of
385 filamentous phages do not encode a secretin, but rather hijack one from their bacterial
386 host^{48,49}. We predict that the outermost hydrophobic girdle in f1pIV forms the membrane
387 embedded domain, as has been proposed for other secretin structures^{17,19,20,43}. The other
388 hydrophobic girdle (located half way down the barrel) would then lie within the periplasm, in
389 a similar position to where pilotins are seen to bind to other secretins (Supplementary Fig.
390 10)⁵⁰. The fact that this hydrophobic girdle has been evolutionarily maintained in f1pIV, even
391 in the absence of a viral pilotin, highlights its functional importance. In support of this, the C-
392 terminus of f1pIV is in close vicinity to the girdle, and C-terminal His-tags result in non-
393 functional f1pIV⁴⁵. In addition, chimeras of f1pIV with C-terminal pilotin-binding S-domains
394 from other secretins (PulD and InvG) are only targeted to the OM and functional for phage
395 assembly in the presence of their respective pilotins (PulS or InvH)^{51,52}. The C-terminus and
396 hydrophobic girdle are thus an important interaction surface, with one possibility being that

397 the phage system is able to hijack bacterial pilotins, or pilotin-like proteins, to aid its
398 targeting and assembly.

399

400 Uptake of hydrophilic and amphipathic antibiotics have been tested with f1pIV previously,
401 whereas hydrophobic drugs have not. We demonstrate that the leaky mutant f1pIV^{S324G}
402 allows *E. coli* to accumulate the hydrophobic macrolide roxithromycin to a greater extent
403 than its wild type counterpart. Ser 324 mutation to Gly likely destroys important hydrogen
404 bonds and alters the position of the peptide backbone, resulting in a more open gate structure
405 that is non-selective to the hydrophobicity of the molecule passing through. These findings,
406 along with our f1pIV atomic model and the conserved nature of secretins, supports targeting
407 the secretin family as an antimicrobial approach^{53,54}. For example, *in silico* and *in vivo*
408 screens could be used to identify molecules that can destabilise the gates, in effect sensitising
409 any secretin-expressing pathogen to a wide range of antibiotics. Phage therapy is also
410 receiving renewed attention, and filamentous phages have been engineered to carry lethal
411 genes to bacteria⁵⁵⁻⁵⁷. Leaky f1pIV could be cloned into the genome of phages of interest, and
412 on protein expression channels would open in the host bacterial outer membrane, allowing
413 antibiotics to enter. Both of these approaches would add much needed artillery to our library
414 of therapeutic tools needed to combat the increasing rise of antimicrobial resistance.

415

416 **Methods**

417 The system of amino acid numbering used throughout is for the mature wild-type f1pIV
418 protein (minus the 21 signal sequence residues). Standard reagents were purchased from
419 Sigma-Aldrich unless otherwise stated.

420

421 **Bacterial strains**

422 All bacterial strains used were *E. coli* K12 derivatives. TG1 electrocompetent cells were
423 purchased from Lucigen and used for expression of f1pIV for cryoEM studies. Strain K2040
424 [MC4100 *ΔlamB106 degP41* (Δ PstI-Km^R)] described in²⁴ was used for the microfluidics
425 experiments.

426

427 **Expression and purification of f1pIV**

428 His-tagged f1pIV was recombinantly expressed in *E. coli* and purified in the presence of
429 CHAPS detergent (Melford) based on previously published methods^{37,58}. The wild type
430 protein was engineered to have a 9 residue His tag (SAHHHHHHH) inserted at position 308
431 and a stabilizing S318I mutation⁴⁵. Protein expression was induced overnight at 20°C and
432 cells were lysed by sonication. The membrane fraction was solubilized in 5% (w/v) CHAPS,
433 50 mM Tris pH 7.6, 500 mM NaCl, 30 mM imidazole and incubated with Ni²⁺ Sepharose
434 beads. f1pIV was eluted with a 0.03-1 M imidazole gradient, and then further purified by gel
435 filtration chromatography on a Superose 6 Increase 10/300 GL column (GE Healthcare) in
436 1% (w/v) CHAPS, 25 mM Na HEPES pH 8.0, 500 mM NaCl, 0.5 mM EDTA. Purified f1pIV
437 was separated on an Any kD mini-protean TGX gel (Biorad), electrophoretically transferred
438 to PVDF membrane and incubated with an anti-pIV antibody.

439

440 **Cryo-EM grid preparation and data collection**

441 The f1pIV purified sample (3 μ l of ~0.7mg/ml) was applied to graphene oxide-coated lacey
442 carbon grids, 300 mesh (Agar Scientific) without any glow discharge, and frozen on a Mark
443 IV Vitrobot (Thermo Fisher Scientific, 4°C, 100% relative humidity, blot force 0, blot time 4
444 sec). Micrographs were collected on a 300 kV Titan Krios microscope (Thermo Fisher
445 Scientific) with a K3 direct electron detector (Gatan) at the Electron Bio-imaging Centre
446 (eBIC) at Diamond Light Source, UK. Data were collected using EPU software with a pixel

447 size of 1.072 Å (0.536 Å super-resolution) and a defocus range from -2.5 µm to -1.3 µm.
448 Further details are shown in Supplementary Table 1. A subset of data was collected in normal
449 mode (dataset 1), and a second subset in super-resolution mode (dataset 2).

450

451 **Cryo-EM image processing**

452 Warp⁵⁹ was used for motion correction, CTF correction and particle picking. 241,591
453 particles were picked from 7037 micrographs for dataset 1 and 330,389 from 14,336 for
454 dataset 2. Both sets of data were processed separately and combined in the latter stages of
455 data processing. Several rounds of 2D classification and 3D refinement were implemented in
456 Relion²³ followed by CTF refinement and polishing steps. The statistics of data collection and
457 model reconstruction are shown in Supplementary Table 1, and data quality checks^{60,61} are
458 shown in Supplementary Fig. 2.

459

460 **Model building and refinement**

461 A homologous structure of the Type II secretin GspD from Enteropathogenic *Escherichia*
462 *coli* (5W68) was manually placed in the cryoEM map using Chimera⁶². Subsequent building
463 and model adjustments were performed using Coot⁶³. Bulky residues, glycine residues and
464 unique sequence patterns were used to guide sequence assignment during model building. 15-
465 fold symmetry was applied in Chimera, and the multimeric structure was refined using
466 Refmac from the CCPEM suite⁶⁴, with the quality of the model evaluated using the validation
467 tools in Coot and Molprobit⁶⁵. DeepEMhancer⁶⁶ was used for denoising and postprocessing
468 of the maps, which were then analysed to check for additional information that could be
469 modelled from the improved maps. A Fourier Shell Correlation (FSC) curve showing the
470 quality of the model to map fit (calculated with Phenix)⁶¹ is shown in Supplementary Fig. 2.

471

472 **Mass spectrometry analysis**

473 A sample of f1pIV was run on an SDS-PAGE gel (Any kD mini-protean TGX, Biorad),
474 stained with Coomassie, and the band of interest excised with a sterile scalpel blade. The gel
475 band was subjected to in-gel tryptic digestion using a DigestPro automated digestion unit
476 (Intavis Ltd.) and the resulting peptides were fractionated using an Ultimate 3000 nano-LC
477 system in line with an Orbitrap Fusion Tribrid mass spectrometer (Thermo Scientific). In
478 brief, peptides in 1% (vol/vol) formic acid were injected onto an Acclaim PepMap C18 nano-
479 trap column (Thermo Scientific). After washing with 0.5% (vol/vol) acetonitrile 0.1%
480 (vol/vol) formic acid peptides were resolved on a 250 mm × 75 µm Acclaim PepMap C18
481 reverse phase analytical column (Thermo Scientific) over a 150 min organic gradient, using 7
482 gradient segments (1-6% solvent B over 1 min., 6-15% B over 58 min., 15-32%B over 58
483 min., 32-40%B over 5 min., 40-90%B over 1 min., held at 90%B for 6min and then reduced
484 to 1%B over 1min.) with a flow rate of 300 nl min⁻¹. Solvent A was 0.1% formic acid and
485 Solvent B was aqueous 80% acetonitrile in 0.1% formic acid. Peptides were ionized by nano-
486 electrospray ionization at 2.2 kV using a stainless-steel emitter with an internal diameter of
487 30 µm (Thermo Scientific) and a capillary temperature of 250°C.

488 All spectra were acquired using an Orbitrap Fusion Tribrid mass spectrometer controlled by
489 Xcalibur 2.1 software (Thermo Scientific) and operated in data-dependent acquisition mode.
490 FTMS1 spectra were collected at a resolution of 120 000 over a scan range (m/z) of 350-
491 1550, with an automatic gain control (AGC) target of 400 000 and a max injection time of
492 100ms. Precursors were filtered according to charge state (to include charge states 2-7), with
493 monoisotopic peak determination set to peptide and using an intensity range from 5E3 to
494 1E20. Previously interrogated precursors were excluded using a dynamic window (40 s +/-10
495 ppm). The MS2 precursors were isolated with a quadrupole mass filter set to a width of 1.6

496 m/z. ITMS2 spectra were collected with an AGC target of 5000, max injection time of 50 ms
497 and HCD collision energy of 35%.

498 The raw data files were processed and quantified using Proteome Discoverer software v1.4
499 (Thermo Scientific) and searched against the UniProt *Escherichia coli* database (4349
500 sequences) plus the supplied amino acid sequence using the SEQUEST algorithm. Peptide
501 precursor mass tolerance was set at 10 ppm, and MS/MS tolerance was set at 0.8 Da. Search
502 criteria included carbamidomethylation of cysteine (+57.0214) as a fixed modification and
503 oxidation of methionine (+15.9949) as a variable modification. Searches were performed
504 with full tryptic digestion and a maximum of 1 missed cleavage was allowed. The reverse
505 database search option was enabled and all peptide data was filtered to satisfy false discovery
506 rate (FDR) of 5%.

507 **Sequence alignments and homology modelling**

508 The sequence of the N terminal region of the model that was not accounted for in our
509 structure (residues 1-107) was subjected to a Blast search⁶⁷ against all sequences in the
510 Protein Data Bank. A sequence alignment of the top hit was performed on f1pIV with
511 Praline⁶⁸ and Swiss-Model²⁵ used to create a homology model of the f1pIV N0 domain. In
512 addition, the sequence of the f1pIV N0 domain was submitted to the I-TASSER structural
513 prediction server²⁶ (which gave 5 top models based on a number of different sequences), and
514 also to the Robetta structural prediction server²⁷ (which also produced 5 top models). All
515 models were in agreement for residues 1-71 where they started to diverge. Open and closed
516 gate structures of InvG from *Salmonella typhimurium* were superimposed with the closed
517 structure of f1pIV, and Gate 1 and 2 loops were modelled into an open position using Coot.
518 15-fold symmetry was applied to produce a model of the f1pIV open state.

519

520 The Consurf server⁴⁴ was used to perform a sequence alignment of f1pIV homologues (101
521 unique sequences with 35-100% homology from the Uni-Prot database were used for this
522 analysis), map them to the f1pIV structure and colour them by the degree of sequence
523 conservation.

524

525 **Determination of minimum inhibitory concentration**

526 *E. coli* cells were freshly transformed with plasmid pPMR132^{WT} or pPMR132^{S324G} and single
527 colonies of *E. coli* f1pIV^{WT} or *E. coli* f1pIV^{S324G} were picked and cultured at 37 °C in FB
528 media (2.5% (w/v) tryptone, 0.75% (w/v) yeast extract, 0.6% (w/v) NaCl, 0.1% (w/v)
529 glucose, 50 mM TrisHCl (pH 7.5)). Plasmid DNA was minipreped and sequenced for each
530 experiment to ensure there had been no additional mutations. Protein expression was induced
531 overnight (in FB media plus 0.5 mg/ml bovine serum albumin) with 1mM IPTG at 20 °C,
532 then diluted 40-fold and grown to OD₆₀₀ = 0.5. 60 µl of roxithromycin stock (640 µg/ml in
533 DMSO) were added to the first column of a 96-well plate. 40 µl of the induction media (FB
534 media, 1mM IPTG, 0.5 mg/ml BSA) was added to the first column, and 30 µl to all other
535 wells. 70 µl solution was then withdrawn from the first column and serially transferred to the
536 next column until 70 µl solution withdrawn from the last column was discharged. The mid-
537 log phase cultures (i.e. OD₆₀₀ = 0.5) were diluted to 10⁶ colony forming units (c.f.u.)/ml and
538 30 µl was added to each well, to give a final concentration of 5×10⁵ c.f.u./ml. Each plate
539 contained two rows of 12 positive control experiments (i.e. bacteria growing in induction
540 media without roxithromycin) and two rows of 12 negative control experiments (i.e.
541 induction media only). Plates were incubated at 37 °C overnight. The minimum inhibitory
542 concentrations (MICs) of roxithromycin against *E. coli* f1pIV^{WT} and *E. coli* f1pIV^{S324G} were
543 determined visually, with the MIC being the lowest concentration well with no visible growth
544 (compared to the positive control experiments).

545

546 **Single-cell microfluidics**

547 Single-cell microfluidics experiments to measure the intracellular accumulation of
548 roxithromycin-NBD were carried out as previously reported^{38,40,42}. Briefly, overnight cultures
549 were prepared as described above and a 50 ml aliquot was centrifuged for 5 min at 4000 rpm
550 and 37 °C and resuspended at an OD₅₉₅ of 75. A 2 µl aliquot of this suspension was injected
551 in the microfluidic mother machine device and incubated at 37 °C. The microfluidic device
552 was completed by the integration of fluorinated ethylene propylene tubing (1/32" × 0.008").
553 The inlet tubing was connected to the inlet reservoir which was connected to a computerised
554 pressure-based flow control system (MFCS-4C, Fluigent). The microfluidic device was
555 mounted on an inverted microscope (IX73 Olympus, Tokyo, Japan) and the main
556 microchamber of the mother machine was washed into the waste reservoir by flowing media
557 at 100 µl/h for 2 h. Images were collected via a 60×, 1.2 N.A. objective (UPLSAPO60XW,
558 Olympus) and a sCMOS camera (Zyla 4.2, Andor, Belfast, UK). After this initial 2 h growth
559 period in growth media, the microfluidic environment was changed by flowing media
560 containing roxithromycin-NBD at a concentration of 46 µg/ml. Upon acquiring a bright-field
561 image the microscope was switched to fluorescent mode and FITC filter using custom built
562 Labview software. A fluorescence image was acquired by exposing the bacteria to the blue
563 excitation band of a broad-spectrum LED (CoolLED pE300white, Andover, UK) at 20% of
564 its intensity. Bright-field and fluorescence imaging was carried out every 10 min. The entire
565 assay was carried out at 37 °C in an environmental chamber (Solent Scientific, Portsmouth,
566 UK) surrounding the microscope and microfluidics equipment. Images were processed as
567 previously described^{38,40,42}.

568

569 **Data availability**

570 Density maps of f1pIV have been deposited in the Electron Microscopy Data Bank (EMDB,
571 <https://www.ebi.ac.uk/pdbe/emdb/>) with entry code EMD-12874. A model of f1pIV has been
572 deposited in the Protein Data Bank (PDB, <https://www.rcsb.org/>) with accession number
573 7OFH.

574

575 **Acknowledgements**

576 This work was funded by a Wellcome Trust Seed Award in Science awarded to V.G.
577 (210363/Z/18/Z), which along with the University of Exeter, supported R.C. M.M and K.S.
578 were supported by a BBSRC responsive mode grant awarded to V.G. (BB/R008639/1). U.L.
579 was supported through a BBSRC responsive mode grant (BB/V008021/1), an MRC
580 Proximity to Discovery EXCITEME2 grant (MCPC17189) and an award from the Gordon
581 and Betty Moore Foundation Marine Microbiology Initiative (GBMF5514) awarded to S.P.
582 M.R.L.S. was supported by an Australian Postgraduate Award (APA), PhD scholarship and
583 an IMB Research Advancement Award. We acknowledge Diamond Light Source for access
584 and support of the cryo-EM facilities at the UK's national Electron Bio-imaging Centre
585 (eBIC) at Diamond Light Source [under proposal BI25452], funded by the Wellcome Trust,
586 MRC and BBRSC. We acknowledge access and support of the GW4 Facility for High-
587 Resolution Electron Cryo-Microscopy, funded by the Wellcome Trust (202904/Z/16/Z and
588 206181/Z/17/Z) and BBSRC (BB/R000484/1). The deposited dataset was collected at eBIC,
589 and the GW4 facility was used for sample screening. We are grateful to Ufuk Borucu of the
590 GW4 Regional Facility for High-Resolution Electron Cryo-Microscopy for help with
591 screening, Kate Heesom of University of Bristol Proteomics Facility for the mass
592 spectrometry analysis, and to Marjorie Russel for valuable comments on the manuscript,
593 advice, and her generous gifts of the f1pIV expression vectors (pPMR132 and
594 pPMR132S324G) and anti-f1pIV antibody.

595

596 **Author contributions**

597 R.C. expressed and purified the protein, prepared samples for cryoEM, processed cryoEM
598 data, built the atomic model, interpreted results and prepared figures. M.M. collected and
599 processed cryoEM data. U.L. performed microfluidics experiments and analysed single-cell
600 data. K.S. prepared samples for single-cell microfluidic experiments and supported R.C. S.P.
601 designed single-cell microfluidics experiments. M.R.L.S and M.A.T.B designed and
602 synthesised the macrolide fluorescent probes used in the microfluidics experiments. B.D.
603 interpreted data. J.R. and V.A.M.G. conceptualised the project; V.A.M.G. designed the
604 research, obtained funding for the project and wrote the manuscript with R.C. All authors
605 commented on the manuscript.

606

607 **Competing interests statement**

608 The authors declare no competing interests.

609

610 **References**

- 611 1 Marvin, D. A., Symmons, M. F. & Straus, S. K. Structure and assembly of
612 filamentous bacteriophages. *Prog Biophys Mol Biol* **114**, 80-122,
613 doi:10.1016/j.pbiomolbio.2014.02.003 (2014).
- 614 2 Rakonjac, J. Filamentous Bacteriophages: Biology and Applications. *eLS*, 1-13,
615 doi:10.1002/9780470015902.a0000777 (2012).
- 616 3 Szot-Karpińska, K. *et al.* Modified Filamentous Bacteriophage as a Scaffold for
617 Carbon Nanofiber. *Bioconjugate Chemistry* **27**, 2900-2910,
618 doi:10.1021/acs.bioconjchem.6b00555 (2016).
- 619 4 Mao, C. *et al.* Virus-Based Toolkit for the Directed Synthesis of Magnetic and
620 Semiconducting Nanowires. *Science* **303**, 213-217, doi:10.1126/science.1092740
621 (2004).
- 622 5 Nathan, C. Resisting antimicrobial resistance. *Nature Reviews Microbiology* **18**, 259-
623 260, doi:10.1038/s41579-020-0348-5 (2020).
- 624 6 McKenna, M. The antibiotic paradox: why companies can't afford to create life-
625 saving drugs. *Nature* **584**, 338-341, doi:10.1038/d41586-020-02418-x (2020).
- 626 7 Brives, C. & Pourraz, J. Phage therapy as a potential solution in the fight against
627 AMR: obstacles and possible futures. *Palgrave Communications* **6**, 1-11,
628 doi:10.1057/s41599-020-0478-4 (2020).

- 629 8 Hampton, H. G., Watson, B. N. J. & Fineran, P. C. The arms race between bacteria
630 and their phage foes. *Nature* **577**, 327-336, doi:10.1038/s41586-019-1894-8 (2020).
- 631 9 Rakonjac, J., Bennett, N. J., Spagnuolo, J., Gagic, D. & Russel, M. Filamentous
632 bacteriophage: biology, phage display and nanotechnology applications. *Current*
633 *issues in molecular biology* **13**, 51-76, doi:10.21775/cimb.013.051 (2011).
- 634 10 Riechmann, L. & Holliger, P. The C-terminal domain of TolA is the coreceptor for
635 filamentous phage infection of E. coli. *Cell* **90**, 351-360, doi:10.1016/S0092-
636 8674(00)80342-6 (1997).
- 637 11 Hay, I. D. & Lithgow, T. Filamentous phages: masters of a microbial sharing
638 economy. *EMBO reports* **20**, doi:10.15252/embr.201847427 (2019).
- 639 12 Russel, M. & Kazmierczak, B. Analysis of the structure and subcellular location of
640 filamentous phage pIV. *Journal of Bacteriology* **175**, 3998-4007,
641 doi:10.1128/jb.175.13.3998-4007.1993 (1993).
- 642 13 Feng, J. n., Model, P. & Russel, M. A trans-envelope protein complex needed for
643 filamentous phage assembly and export. *Molecular Microbiology* **34**, 745-755,
644 doi:10.1046/j.1365-2958.1999.01636.x (1999).
- 645 14 Green, E. R. & Meccas, J. Bacterial Secretion Systems: An Overview. *Microbiology*
646 *Spectrum* **4**, 1-32, doi:10.1128/microbiolspec.vmbf-0012-2015 (2016).
- 647 15 D'Imprima, E. *et al.* Cryo-EM structure of the bifunctional secretin complex of
648 *Thermus thermophilus*. *eLife* **6**, 1-23, doi:10.7554/eLife.30483 (2017).
- 649 16 Hu, J. *et al.* Cryo-EM analysis of the T3S injectisome reveals the structure of the
650 needle and open secretin. *Nature Communications* **9**, 1-11, doi:10.1038/s41467-018-
651 06298-8 (2018).
- 652 17 Hay, I. D., Belousoff, M. J., Dunstan, R. A., Bamert, R. S. & Lithgow, T. Structure
653 and membrane topography of the vibrio-type secretin complex from the type 2
654 secretion system of enteropathogenic *Escherichia coli*. *Journal of Bacteriology* **200**,
655 1-15, doi:10.1128/JB.00521-17 (2018).
- 656 18 Yin, M., Yan, Z. & Li, X. Structural insight into the assembly of the type II secretion
657 system pilotin-secretin complex from enterotoxigenic *Escherichia coli*. *Nature*
658 *Microbiology* **3**, 581-587, doi:10.1038/s41564-018-0148-0 (2018).
- 659 19 Filloux, A. & Voulhoux, R. Multiple structures disclose the secretins' secrets. *Journal*
660 *of Bacteriology* **200**, 1-5, doi:10.1128/JB.00702-17 (2018).
- 661 20 Majewski, D. D., Worrall, L. J. & Strynadka, N. C. J. Secretins revealed: structural
662 insights into the giant gated outer membrane portals of bacteria. *Current Opinion in*
663 *Structural Biology* **51**, 61-72, doi:10.1016/j.sbi.2018.02.008 (2018).
- 664 21 Naskar, S., Hohl, M., Tassinari, M. & Low, H. H. The structure and mechanism of the
665 bacterial type II secretion system. *Molecular Microbiology* **115**, 412-424,
666 doi:10.1111/mmi.14664 (2021).
- 667 22 Opalka, N. *et al.* Structure of the filamentous phage pIV multimer by cryo-electron
668 microscopy. *Journal of Molecular Biology* **325**, 461-470, doi:10.1016/S0022-
669 2836(02)01246-9 (2003).
- 670 23 Zivanov, J. *et al.* New tools for automated high-resolution cryo-EM structure
671 determination in RELION-3. *eLife* **7**, 1-22, doi:10.7554/eLife.42166 (2018).
- 672 24 Spagnuolo, J. *et al.* Identification of the gate regions in the primary structure of the
673 secretin pIV. *Molecular Microbiology* **76**, 133-150, doi:10.1111/j.1365-
674 2958.2010.07085.x (2010).
- 675 25 Waterhouse, A. *et al.* SWISS-MODEL: Homology modelling of protein structures
676 and complexes. *Nucleic Acids Research* **46**, W296-W303, doi:10.1093/nar/gky427
677 (2018).

- 678 26 Yang, J. *et al.* The I-TASSER suite: Protein structure and function prediction. *Nature*
679 *Methods* **12**, 7-8, doi:10.1038/nmeth.3213 (2014).
- 680 27 Baek, M. *et al.* Accurate prediction of protein structures and interactions using a 3-
681 track network. *bioRxiv*, 1-17, doi:10.1101/2021.06.14.448402 (2021).
- 682 28 Chernyatina, A. A. & Low, H. H. Core architecture of a bacterial type II secretion
683 system. *Nature Communications* **10**, 1-10, doi:10.1038/s41467-019-13301-3 (2019).
- 684 29 Vollmer, W. & Seligman, S. J. Architecture of peptidoglycan: more data and more
685 models. *Trends in Microbiology* **18**, 59-66, doi:10.1016/j.tim.2009.12.004 (2010).
- 686 30 Chaptal, V. *et al.* Quantification of Detergents Complexed with Membrane Proteins.
687 *Scientific Reports* **7**, 1-12, doi:10.1038/srep41751 (2017).
- 688 31 Schulz, G. E. β -barrel membrane proteins. *Current Opinion in Structural Biology* **10**,
689 443-447, doi:10.1016/S0959-440X(00)00120-2 (2000).
- 690 32 Yan, Z., Yin, M., Xu, D., Zhu, Y. & Li, X. Structural insights into the secretin
691 translocation channel in the type II secretion system. *Nature Structural and Molecular*
692 *Biology* **24**, 177-183, doi:10.1038/nsmb.3350 (2017).
- 693 33 Hu, J. *et al.* T3S injectisome needle complex structures in four distinct states reveal
694 the basis of membrane coupling and assembly. *Nature Microbiology* **4**, 2010-2019,
695 doi:10.1038/s41564-019-0545-z (2019).
- 696 34 Marvin, D. A., Welsh, L. C., Symmons, M. F., Scott, W. R. P. & Straus, S. K.
697 Molecular structure of fd (f1, M13) filamentous bacteriophage refined with respect to
698 X-ray fibre diffraction and solid-state NMR data supports specific models of phage
699 assembly at the bacterial membrane. *Journal of Molecular Biology* **355**, 294-309,
700 doi:10.1016/j.jmb.2005.10.048 (2006).
- 701 35 Russel, M. Mutants at conserved positions in gene IV, a gene required for assembly
702 and secretion of filamentous phages. *Molecular Microbiology* **14**, 357-369,
703 doi:10.1111/j.1365-2958.1994.tb01296.x (1994).
- 704 36 Russel, M., Linderoth, N. A. & Šali, A. Filamentous phage assembly: Variation on a
705 protein export theme. *Gene* **192**, 23-32, doi:10.1016/S0378-1119(96)00801-3 (1997).
- 706 37 Marciano, D. K., Russel, M. & Simon, S. M. An aqueous channel for filamentous
707 phage export. *Science* **284**, 1516-1519, doi:10.1126/science.284.5419.1516 (1999).
- 708 38 Stone, M. R. L. *et al.* Fluorescent macrolide probes – synthesis and use in evaluation
709 of bacterial resistance. *RSC Chemical Biology* **1**, 395-404, doi:10.1039/d0cb00118j
710 (2020).
- 711 39 Bryskier, A. Roxithromycin: Review of its antimicrobial activity. *Journal of*
712 *Antimicrobial Chemotherapy* **41**, 1-21, doi:10.1093/jac/41.suppl_2.1 (1998).
- 713 40 Łapińska, U., Glover, G., Capilla-Lasheras, P., Young, A. J. & Pagliara, S. Bacterial
714 ageing in the absence of external stressors. *Philosophical Transactions of the Royal*
715 *Society B: Biological Sciences* **374**, 1-13, doi:10.1098/rstb.2018.0442 (2019).
- 716 41 Bamford, R. A. *et al.* Investigating the physiology of viable but non-culturable
717 bacteria by microfluidics and time-lapse microscopy. *BMC Biology* **15**, 1-12,
718 doi:10.1186/s12915-017-0465-4 (2017).
- 719 42 Cama, J. *et al.* Single-cell microfluidics facilitates the rapid quantification of
720 antibiotic accumulation in Gram-negative bacteria. *Lab on a Chip* **20**, 2765-2775,
721 doi:10.1039/d0lc00242a (2020).
- 722 43 Weaver, S. J. *et al.* CryoEM structure of the type IVa pilus secretin required for
723 natural competence in *Vibrio cholerae*. *Nature Communications* **11**, 1-13,
724 doi:10.1038/s41467-020-18866-y (2020).
- 725 44 Ashkenazy, H. *et al.* ConSurf 2016: an improved methodology to estimate and
726 visualize evolutionary conservation in macromolecules. *Nucleic acids research* **44**,
727 W344-W350, doi:10.1093/nar/gkw408 (2016).

- 728 45 Linderoth, N. A., Model, P. & Russel, M. Essential role of a sodium dodecyl sulfate-
729 resistant protein IV multimer in assembly-export of filamentous phage. *Journal of*
730 *Bacteriology* **178**, 1962-1970, doi:10.1128/jb.178.7.1962-1970.1996 (1996).
- 731 46 Russel, M. Protein-protein interactions during filamentous phage assembly. *Journal of*
732 *Molecular Biology* **231**, 689-697, doi:10.1006/jmbi.1993.1320 (1993).
- 733 47 Worrall, L. J. *et al.* Near-atomic-resolution cryo-EM analysis of the Salmonella T3S
734 injectisome basal body. *Nature* **540**, 597-601, doi:10.1038/nature20576 (2016).
- 735 48 Davis, B. M. *et al.* Convergence of the secretory pathways for cholera toxin and the
736 filamentous phage, CTX ϕ . *Science* **288**, 333-335, doi:10.1126/science.288.5464.333
737 (2000).
- 738 49 Bille, E. *et al.* A chromosomally integrated bacteriophage in invasive meningococci.
739 *Journal of Experimental Medicine* **201**, 1905-1913, doi:10.1084/jem.20050112
740 (2005).
- 741 50 McCallum, M., Tammam, S., Rubinstein, J. L., Burrows, L. L. & Howell, P. L.
742 CryoEM map of Pseudomonas aeruginosa PilQ enables structural characterization of
743 TsaP. *Structure* **29**, 457-466, doi:10.1016/j.str.2020.11.019 (2021).
- 744 51 Daefler, S., Guilvout, I., Hardie, K. R., Pugsley, A. P. & Russel, M. The C-terminal
745 domain of the secretin PulD contains the binding site for its cognate chaperone, PulS,
746 and confers PulS dependence on pIV(f1) function. *Molecular Microbiology* **24**, 465-
747 475, doi:10.1046/j.1365-2958.1997.3531727.x (1997).
- 748 52 Daefler, S. & Russel, M. The Salmonella typhimurium InvH protein is an outer
749 membrane lipoprotein required for the proper localization of InvG. *Molecular*
750 *Microbiology* **28**, 1367-1380, doi:10.1046/j.1365-2958.1998.00908.x (1998).
- 751 53 Baron, C. & Coombes, B. Targeting Bacterial Secretion Systems: Benefits of
752 Disarmament in the Microcosm. *Infectious Disorders - Drug Targets* **7**, 19-27,
753 doi:10.2174/187152607780090685 (2008).
- 754 54 McShan, A. C. & De Guzman, R. N. The Bacterial Type III Secretion System as a
755 Target for Developing New Antibiotics. *Chemical Biology and Drug Design* **85**, 30-
756 42, doi:10.1111/cbdd.12422 (2015).
- 757 55 Hagens, S. & Bläsi, U. Genetically modified filamentous phage as bactericidal agents:
758 A pilot study. *Letters in Applied Microbiology* **37**, 318-323, doi:10.1046/j.1472-
759 765X.2003.01400.x (2003).
- 760 56 Moradpour, Z. *et al.* Genetically engineered phage harbouring the lethal catabolite
761 gene activator protein gene with an inducer-independent promoter for biocontrol of
762 Escherichia coli. *FEMS Microbiology Letters* **296**, 67-71, doi:10.1111/j.1574-
763 6968.2009.01620.x (2009).
- 764 57 Westwater, C. *et al.* Use of Genetically Engineered Phage To Deliver Antimicrobial
765 Agents to Bacteria: an Alternative Therapy for Treatment of Bacterial Infections.
766 *Antimicrobial Agents and Chemotherapy* **47**, 1301-1307,
767 doi:10.1128/AAC.47.4.1301-1307.2003 (2003).
- 768 58 Linderoth, N. A., Simon, M. N. & Russel, M. The filamentous phage pIV multimer
769 visualized by scanning transmission electron microscopy. *Science* **278**, 1635-1638,
770 doi:10.1126/science.278.5343.1635 (1997).
- 771 59 Tegunov, D. & Cramer, P. Real-time cryo-electron microscopy data preprocessing
772 with Warp. *Nature Methods* **16**, 1146-1152, doi:10.1038/s41592-019-0580-y (2019).
- 773 60 Kucukelbir, A., Sigworth, F. J. & Tagare, H. D. Quantifying the local resolution of
774 cryo-EM density maps. *Nature Methods* **11**, 63-65, doi:10.1038/nmeth.2727 (2014).
- 775 61 Liebschner, D. *et al.* Macromolecular structure determination using X-rays, neutrons
776 and electrons: Recent developments in Phenix. *Acta Crystallographica Section D:*
777 *Structural Biology* **75**, 861-877, doi:10.1107/S2059798319011471 (2019).

- 778 62 Pettersen, E. F. *et al.* UCSF Chimera - A visualization system for exploratory research
779 and analysis. *Journal of Computational Chemistry* **25**, 1605-1612,
780 doi:10.1002/jcc.20084 (2004).
- 781 63 Emsley, P. & Cowtan, K. Coot: Model-building tools for molecular graphics. *Acta*
782 *Crystallographica Section D: Biological Crystallography* **60**, 2126-2132,
783 doi:10.1107/S0907444904019158 (2004).
- 784 64 Wood, C. *et al.* Collaborative computational project for electron cryo-microscopy.
785 *Acta Crystallographica Section D: Biological Crystallography* **71**, 123-126,
786 doi:10.1107/S1399004714018070 (2015).
- 787 65 Williams, C. J. *et al.* MolProbity: More and better reference data for improved all-
788 atom structure validation. *Protein Science* **27**, 293-315, doi:10.1002/pro.3330 (2018).
- 789 66 Sanchez-Garcia, R. *et al.* DeepEMhancer: a deep learning solution for cryo-EM
790 volume post-processing. *bioRxiv*, doi:10.1101/2020.06.12.148296 (2020).
- 791 67 Altschul, S. F., Gish, W., Miller, W., Myers, E. W. & Lipman, D. J. Basic local
792 alignment search tool. *Journal of Molecular Biology* **215**, 403-410,
793 doi:10.1016/S0022-2836(05)80360-2 (1990).
- 794 68 Simossis, V. A. & Heringa, J. PRALINE: A multiple sequence alignment toolbox that
795 integrates homology-extended and secondary structure information. *Nucleic Acids*
796 *Research* **33**, W289-W294, doi:10.1093/nar/gki390 (2005).
797

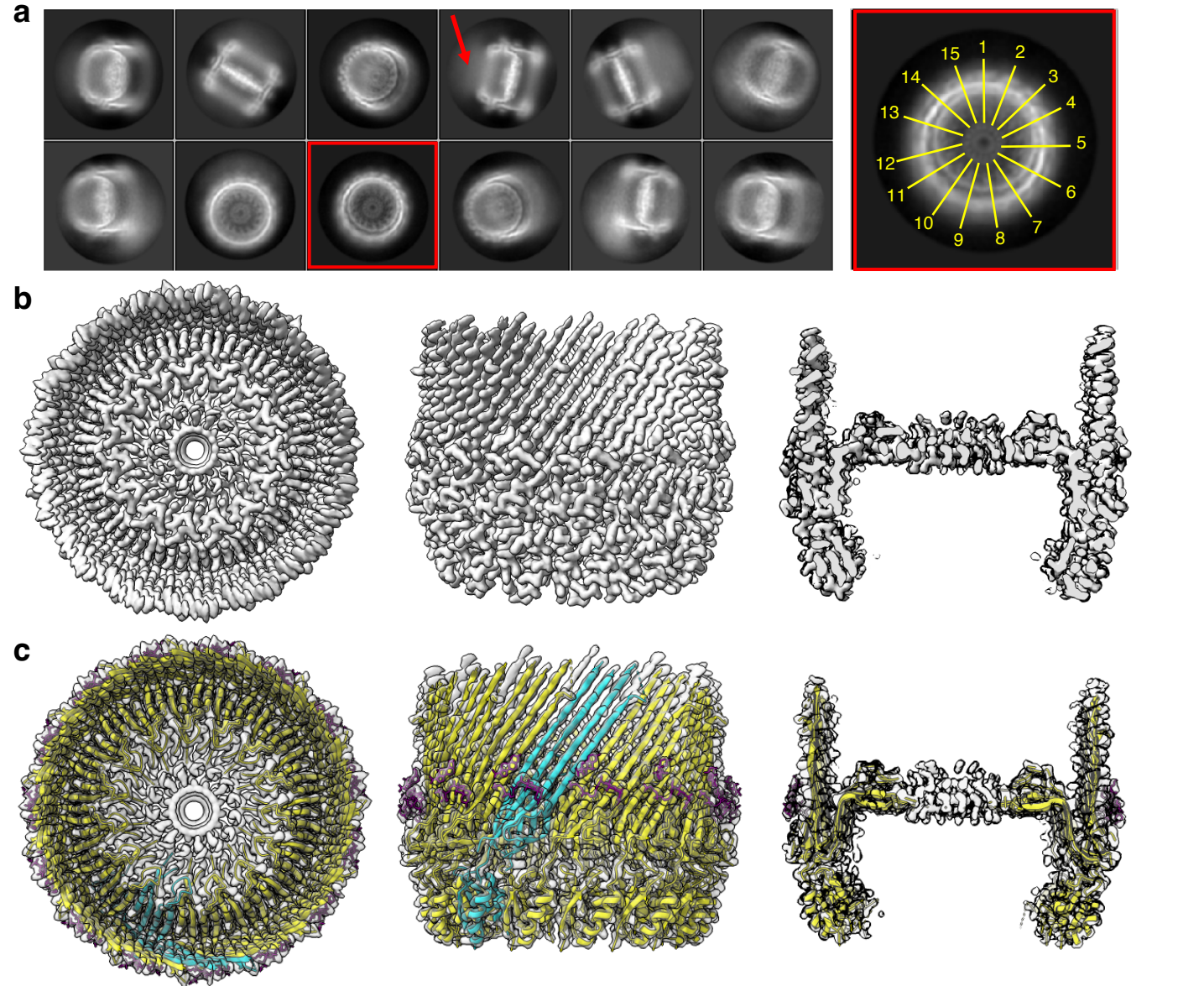


Figure 1. f1pIV cryoEM data and atomic model. a) Left, 2D class averages from Relion. A red arrow highlights a hazy area, likely resulting from protein flexibility. The red box highlights an enlarged top view (right) depicting observed 15-fold symmetry (indicated with yellow lines). **b)** Final 3D reconstruction shown from left to right as top view, side view and side view sliced through the centre. **c)** f1pIV protein structure modelled into the experimental density map shown as a top view, side view and side view sliced through the centre. A single f1pIV monomer is shown as a cyan cartoon with the remaining 14 monomers in yellow; the EM map is shown in light grey. A band of CHAPS detergent molecules are shown as purple sticks. The structure has been deposited with the PDB accession number 7OFH.

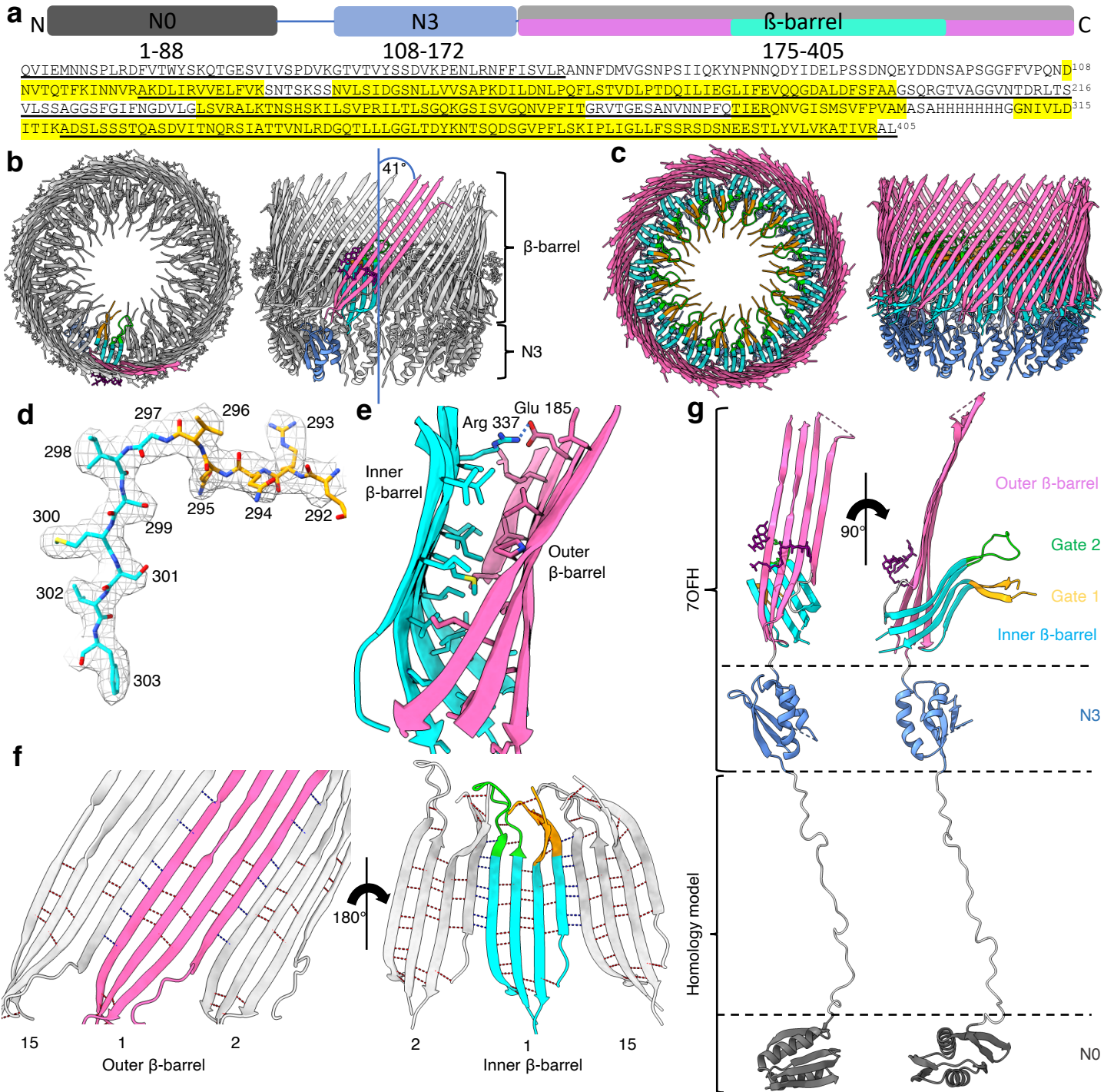


Figure 2. Structural details of flpIV. **a)** Domain structure and amino acid sequence of flpIV, showing the N0 domain (dark grey), the N3 domain (blue), and the secretin domain (light grey). The regions forming the outer β -barrel are shown in pink, and those forming the inner β -barrel in cyan. Residues highlighted in yellow in the amino acid sequence were observed in the cryoEM map and have been modelled into the density. Underlined residues were confirmed to be present in the cryoEM sample by mass spectrometry analysis. **b)** Cartoon representation of the flpIV multimer (top and side views) with a single molecule coloured as follows: N3 domain in blue, outer β -barrel in pink, inner β -barrel in cyan, Gate 1 in orange, Gate 2 in green, and CHAPS molecules as purple sticks. **c)** Cartoon representation of the flpIV multimer with all chains coloured as in **b)**. CHAPS molecules have been removed for clarity. **d)** Residues 292-303 (incorporating part of the Gate 1 loop and the inner β -barrel) showing representative density. **e)** The interface between the inner and outer β -barrels is lined mostly with hydrophobic residues which are shown as sticks, and coloured by atom (N in blue, O in red, S in yellow). A salt bridge is formed at the edge of this interface between conserved residues Glu 185 and Arg 337 (dashed blue line). **f)** Inter- (blue dashed lines) and intra- (red dashed lines) subunit hydrogen bonds are formed connecting the inner and outer β -barrels. One subunit (position 1) is coloured as in **b)**, and the neighbouring subunits (in positions 2 and 15) are shown in grey. Images have been clipped for clarity. **g)** Composite model of the flpIV monomer shown as front and side views. The structure built into the EM map is coloured as in **b)**, with a homology model of the N0 domain in dark grey.

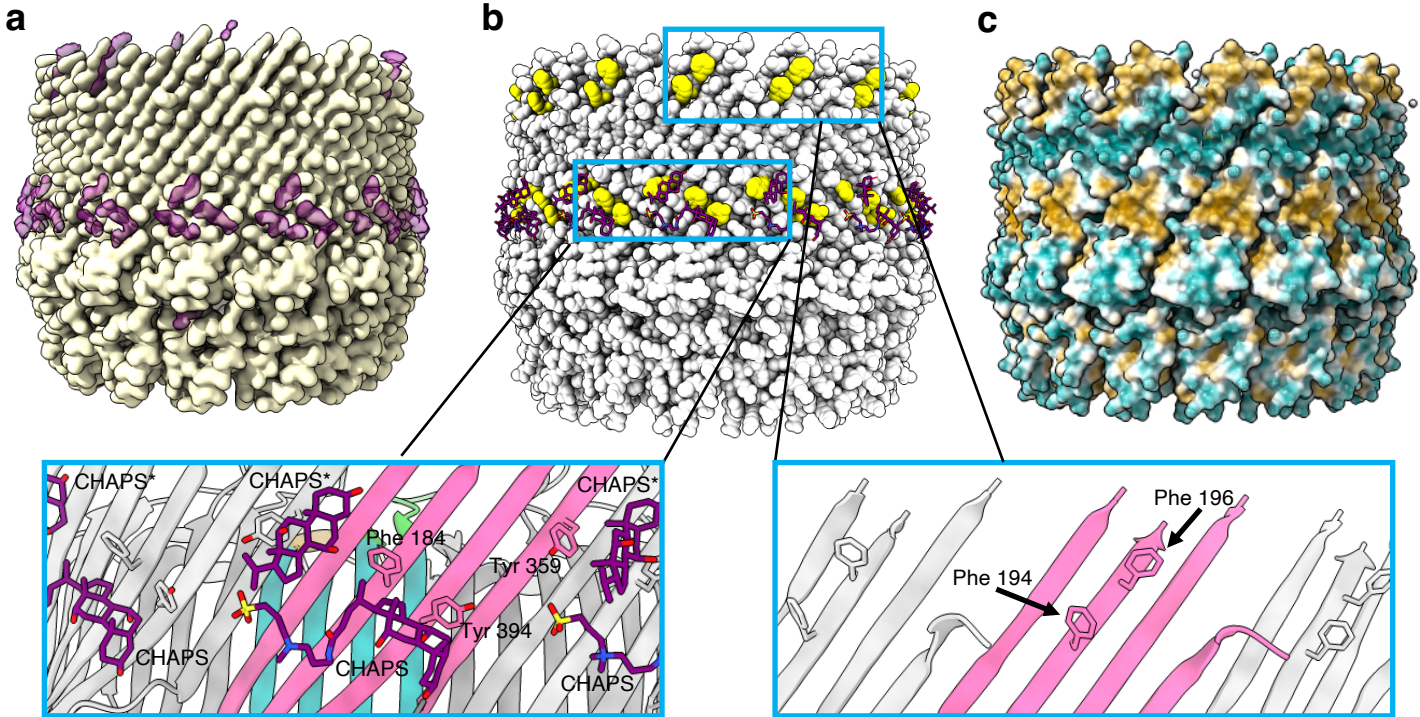


Figure 3. Positioning of the flpIV multimer in the *E. coli* outer membrane. **a)** The flpIV cryoEM map in side view (yellow) shows density that was unaccounted for after the protein had been modelled (purple). **b)** The flpIV atomic model is shown as space-filled atoms in light grey with the CHAPS shown as purple sticks. There are two bands of aromatic residues shown in yellow (aromatic girdles). The enlarged panels (blue boxes) show the two girdles in greater detail with the aromatic residues labelled. One full molecule of CHAPS, and one consisting only of the aromatic rings (CHAPS*) were modelled in to the ring of density. CHAPS is shown as purple sticks, and the flpIV monomers are coloured as in Fig. 2f. **c)** flpIV atomic model shown as surface representation is coloured by hydrophobicity, ranging from the most hydrophilic areas (dark cyan), through white, to the most hydrophobic areas (orange).

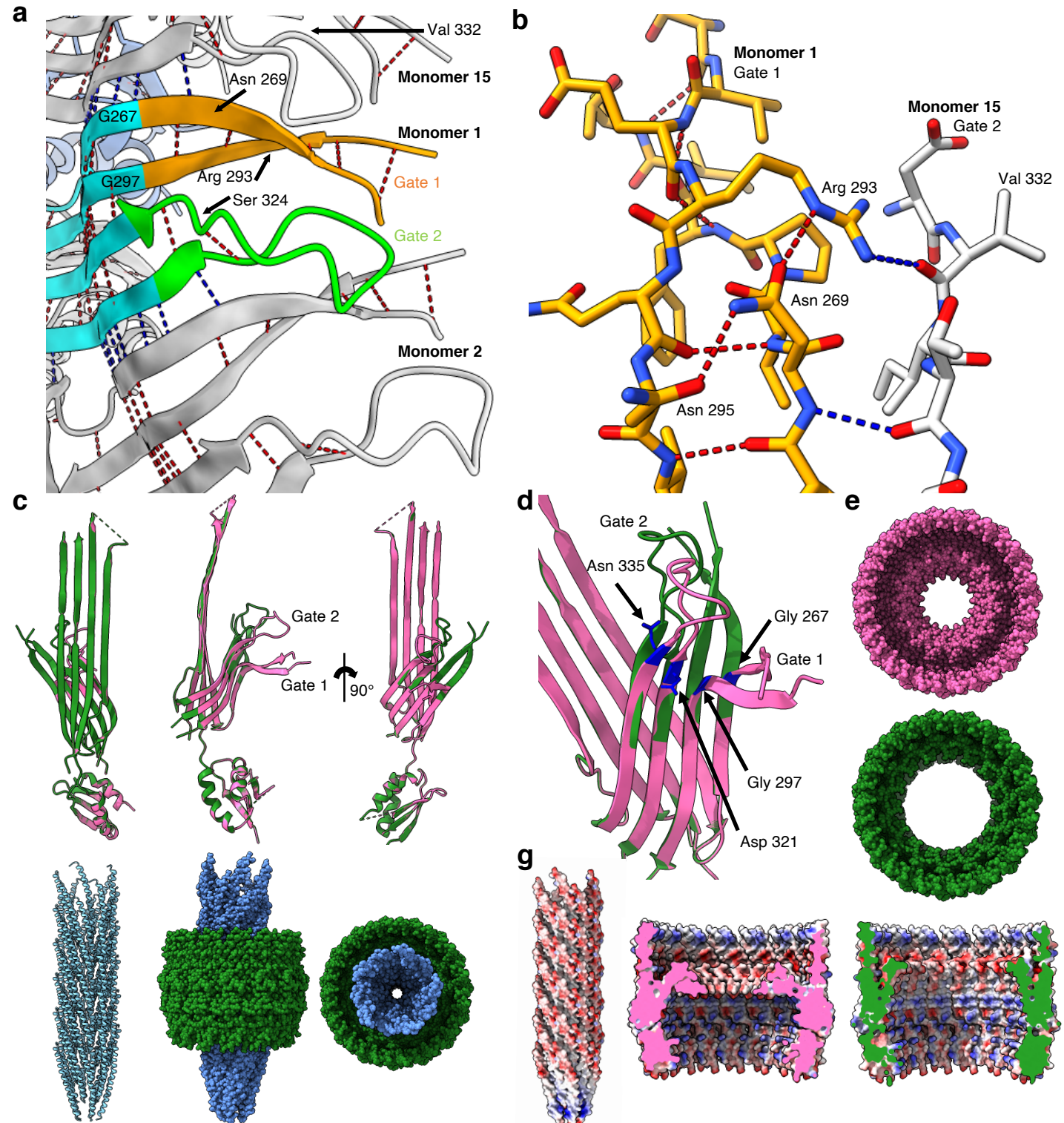


Figure 4. The Gate region, channel opening, and interaction with phage. **a**) Extensive intra- (red dashed lines) and inter- (blue dashed lines) gate hydrogen bonding is seen in Gate 1 and Gate 2, and between neighbouring subunits, colouring as in Fig. 2f. Glycine 267 (G267) and Glycine 297 (G297) hinge residues are shown, along with key residues Asn 269 and Arg 293 in Gate 1, and Ser 324 and Val 332 in Gate 2. **b**) Close up to show the hydrogen bonding interactions of the conserved and buried Arg 293 in Gate 1. Arg 293 forms hydrogen bonds within Gate 1 with a conserved Asn 269, and with Val 332 in Gate 2 of the neighbouring monomer. Gate 1 from monomer 1 is shown in orange and Gate 2 from monomer 15 in grey, and coloured by atom (N in blue, O in red). **c**) Structural superimposition of the flpIV monomer closed state structure (pink) with flpIV modelled in the open gate position (green), shown in front, side and back views. **d**) Close up showing the Gate 1 (Gly 267, Gly 297) and Gate 2 (Asp 321, Asn 335) hinge residues in blue. **e**) The closed (pink) and open (green) multimers shown as space-fill representation in top view. **f**) Left, structure of an fd virion (2C0W) in cartoon form. Centre and right, manual docking of the fd virion (blue space-filled representation) into the open flpIV secretin pore (green surface representation) in side and top views respectively. **g**) Left, electrostatic surface potential of the fd virion coloured red for negative and blue for positive. Centre and right, electrostatic surface potential of the closed (pink) and open (green) states of the flpIV pore, coloured as per the fd virion.

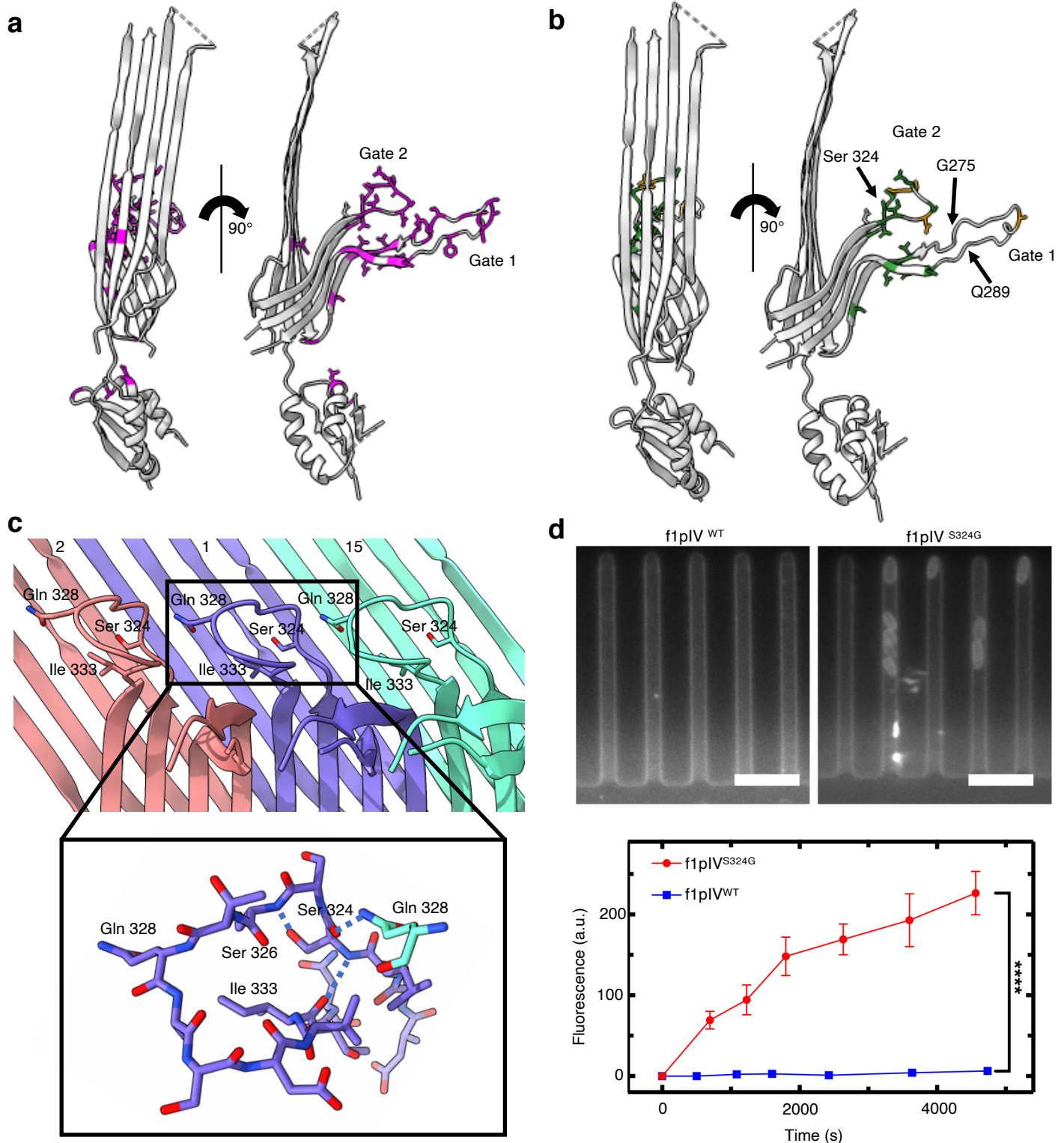


Figure 5. Antibiotic susceptibility in *E. coli* expressing leaky mutants of flpIV. **a)** Front and side views showing all mutants²⁴ that were leaky to both maltopentaose and deoxycholate as magenta sticks. **b)** Front and side views showing the mutations which caused sensitivity to the antibiotics vancomycin and bacitracin as green sticks. Mutations which caused sensitivity to vancomycin only are shown as orange sticks. In parts a) and b) the 15-residue loop from residues G275-Q289 (labelled), which is disordered in our structure, has been modelled in for representation purposes. The position of the Ser 324 mutation to Gly (S324G), analysed in part d), is also shown. **c)** Gate 2 loop showing the key hydrogen bond interactions made by Ser 324. Monomer 1 is shown in purple, with neighbouring monomers 2 and 15 in red and green respectively. The close up shows that Ser 324 forms hydrogen bonds (blue dashed lines) with Ile 333 and Ser 326 within the same monomer, and with Gln 328 from a neighbouring monomer (N in blue, O in red). **d)** Top, individual *E. coli* cells expressing flpIV^{S324G} take up fluorescently labelled roxithromycin. No fluorescence change was observed for the cells expressing wild type flpIV (flpIV^{WT}). Scale bar, 5 μ m. Bottom, scatter graph depicting the fluorescence change for 350 cells for flpIV^{WT} and flpIV^{S324G} samples, confirming roxithromycin uptake in the S324G mutant. Error bars represent standard error of the mean.

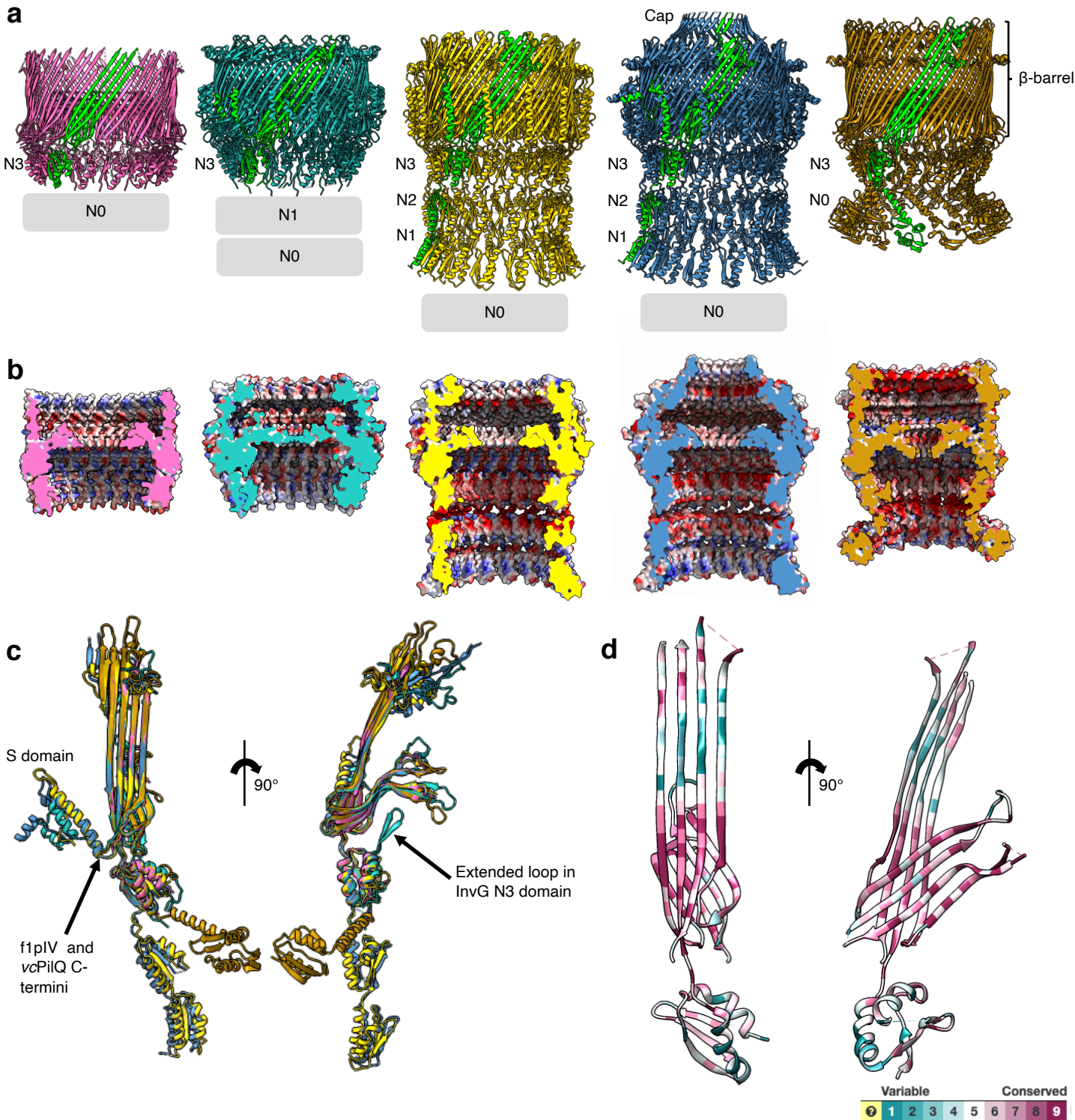


Figure 6. Structural comparison of f1pIV with a selection of different classes of bacterial secretins. Secretins are aligned at the β -barrel domain. f1pIV is shown in pink (this study:7OFH), the Type III secretin InvG from *Salmonella typhimurium* in sea green (6PEE), the Type II secretin GspD from *E. coli* K12 in gold (5WQ7), the Type II secretin GspD from *Vibrio cholerae* in blue (5WQ8) and the Type IV pilus secretin PilQ from *Vibrio cholerae* in orange (6W6M). The secretins are shown in **a**) as multimers (with one monomer coloured lime green). Periplasmic N domains not observed in the maps are shown as grey boxes. **b**) Electrostatic surface potential comparison of multimers cut-through to show the inner surface inside the pore. **c**) Structural superimposition of the selected secretin monomers (shown individually in Supplementary Fig. 8) shown in front (left) and side (right) views. **d**) Sequence conservation amongst the secretin family plotted on to the f1pIV structure, calculated using Consurf and based on 100 unique homologues from the Uni-Prot database sharing 35-100% identity.

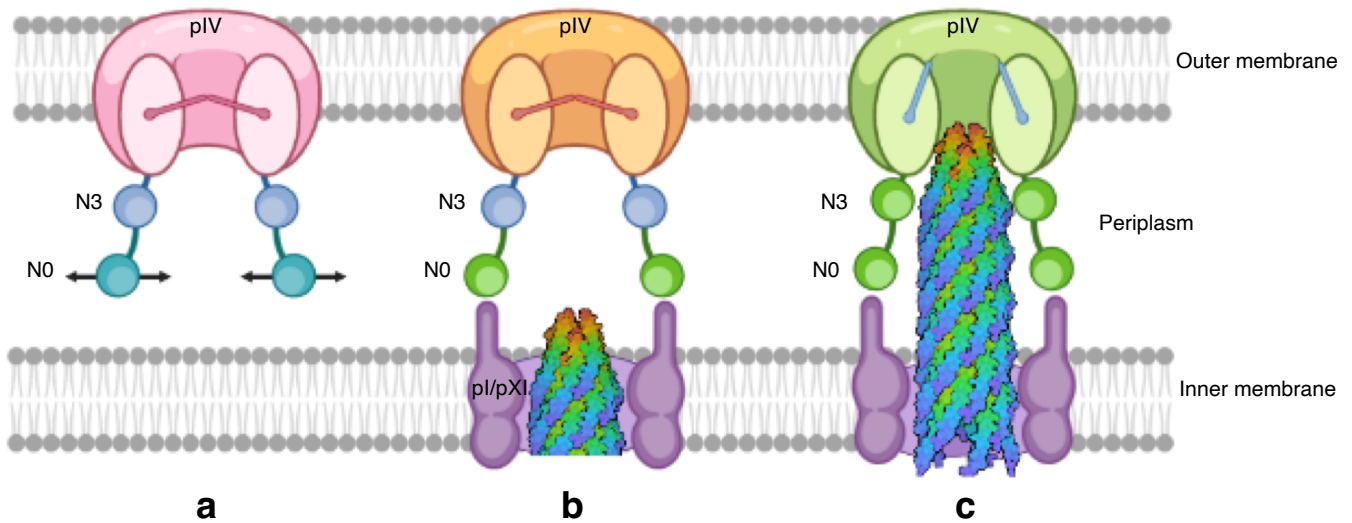
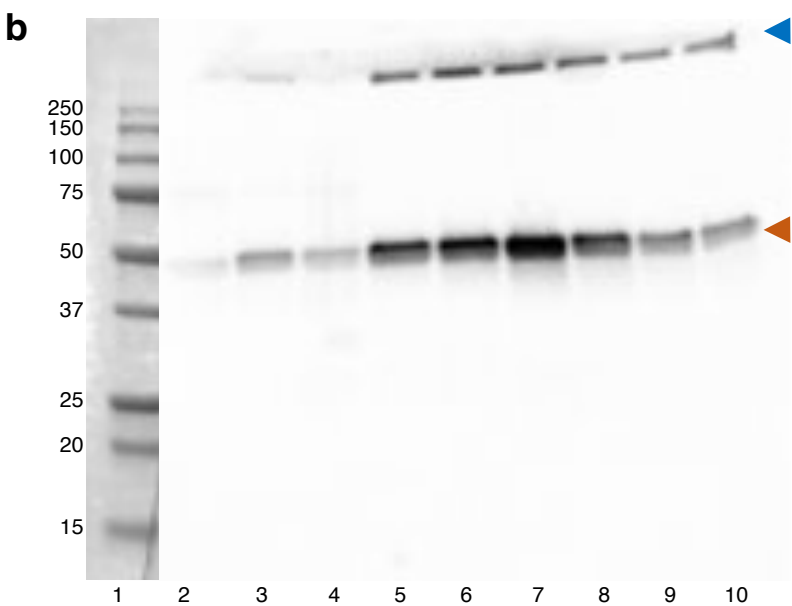
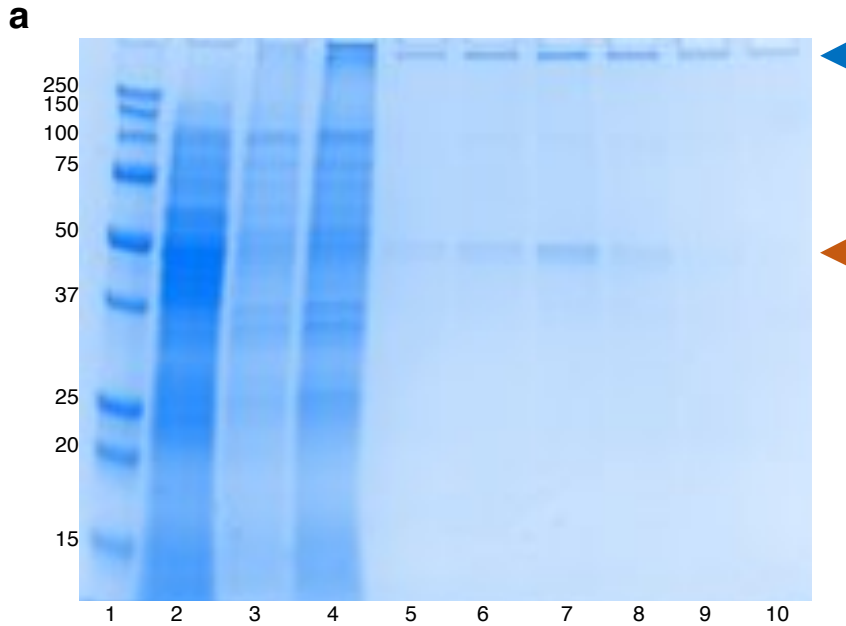


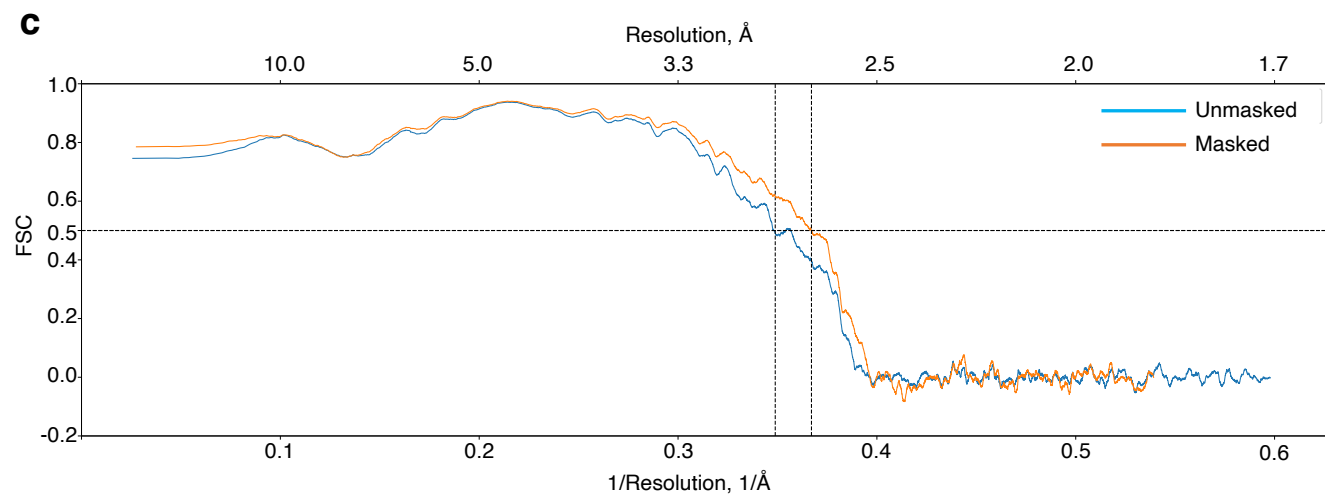
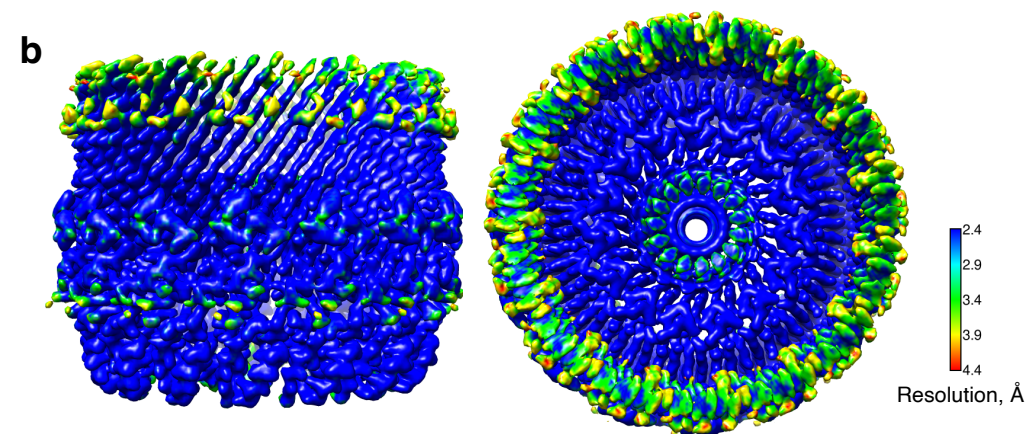
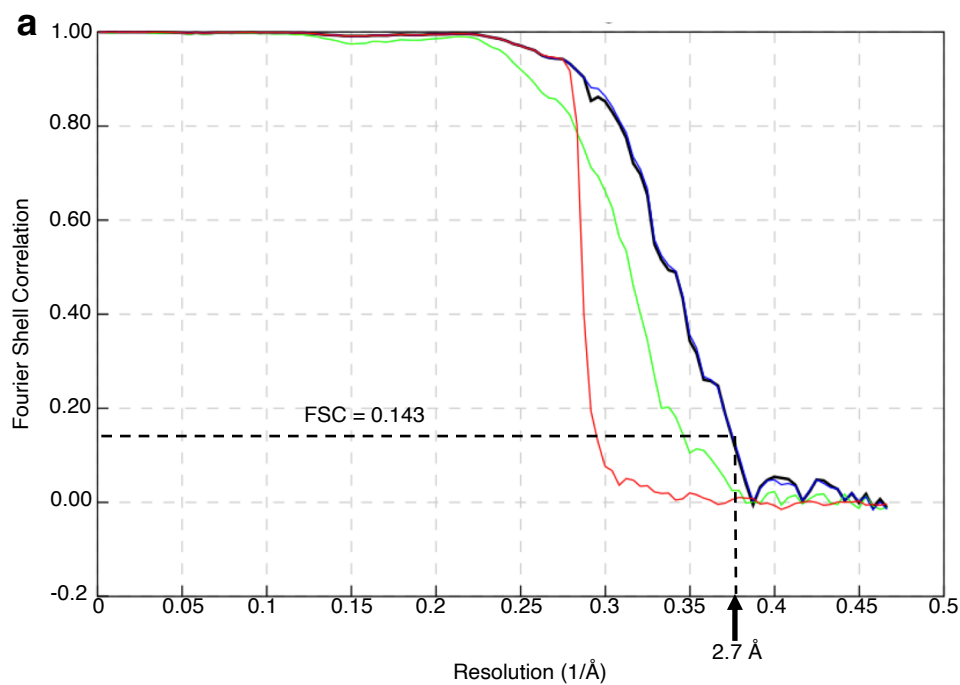
Figure 7. Model for extrusion of filamentous phage. a) f1pIV with the gate in the closed state (pink). The N3 (blue) and N0 (teal) domains project into the periplasm. N0 is attached to N3 via a long linker and is flexible (indicated by black arrows). **b)** N0 (now green, activated) binds to the inner membrane complex of pI/pXI (purple) and the pIV gate (orange) is primed to open. **c)** Egressing phage (blue and green; cap proteins pVII/pIX red and orange) interacts with the N3 domain (now green, activated), triggering opening of pIV (now green, activated) by rearrangement of the gate (blue). Created with [BioRender.com](https://www.biorender.com); the phage was drawn using 2C0W.



c

Accession	Description	Score	Coverage	# proteins	# unique peptides	# peptides	# PSMs	Area	# AAs	MW (kDa)	Calc. pI
f1pIV	f1pIV sequence	2641.11	77.78	1	40	40	973	3.630E11	405	43.4	5.06
POA853	Tryptophanase OS=Escherichia coli (strain K12)	248.61	79.83	1	39	39	91	4.152E9	471	52.7	6.23
POABB4	ATP synthase subunit beta OS=Escherichia coli (strain K12)	180.28	77.61	1	28	28	56	7.750E8	460	50.3	5.01
POABB0	ATP synthase subunit alpha OS=Escherichia coli (strain K12)	120.71	49.32	1	21	22	36	2.840E8	513	55.2	6.13
POA6U8	Glycogen synthase OS=Escherichia coli (strain K12)	118.33	41.93	1	19	19	38	9.668E8	477	52.8	6.62
P13035	Aerobic glycerol-3-phosphate dehydrogenase OS=Escherichia coli (strain K12)	94.42	56.09	1	23	23	32	1.994E8	501	56.7	7.44
POA6F3	Glycerol kinase OS=Escherichia coli (strain K12)	93.32	54.78	1	25	25	32	3.567E8	502	56.2	5.50
P77804	Protein YdgA OS=Escherichia coli (strain K12)	91.30	58.17	1	23	23	29	9.258E7	502	54.7	5.17
POCE47	Elongation factor Tu 1 OS=Escherichia coli (strain K12)	71.19	73.60	2	21	21	27	1.377E8	394	43.3	5.45
POAFG6	Dihydrolipeoyllysine-residue succinyltransferase component of 2-oxoglutarate dehydrogenase complex OS=E. coli (strain K12)	63.11	34.57	1	15	15	20	1.909E8	405	44.0	5.81

Supplementary Figure 1. Purification of f1pIV verified by a) SDS-PAGE and b) Western blot. Lane 1, Biorad Precision Plus All Blue Marker; lane 2, total soluble protein; lane 3, total membrane protein; lane 4, solubilized membrane protein; lanes 5-10, fractions from size exclusion chromatography. The f1pIV monomer is indicated with an orange arrowhead and the multimer by a blue arrowhead. Lane 1 (protein markers) was cut away and visualized with white light, hence the difference in colouring compared to the rest of the blot. **c) Mass spectrometry analysis.** The top ten proteins identified in the mass spectrometry analysis are shown, with f1pIV clearly being the most abundant protein present.



Supplementary Figure 2. f1pIV data quality. a) FSC curve obtained from Relion. The calculated final map was determined at 2.7 \AA resolution using Fourier shell correlation at the 0.143 cut-off.

Red curve = `rlnCorrectedFourierShellCorrelationPhaseRandomizedMaskedMaps`.

Green curve = `rlnFourierShellCorrelationUnmaskedMaps`.

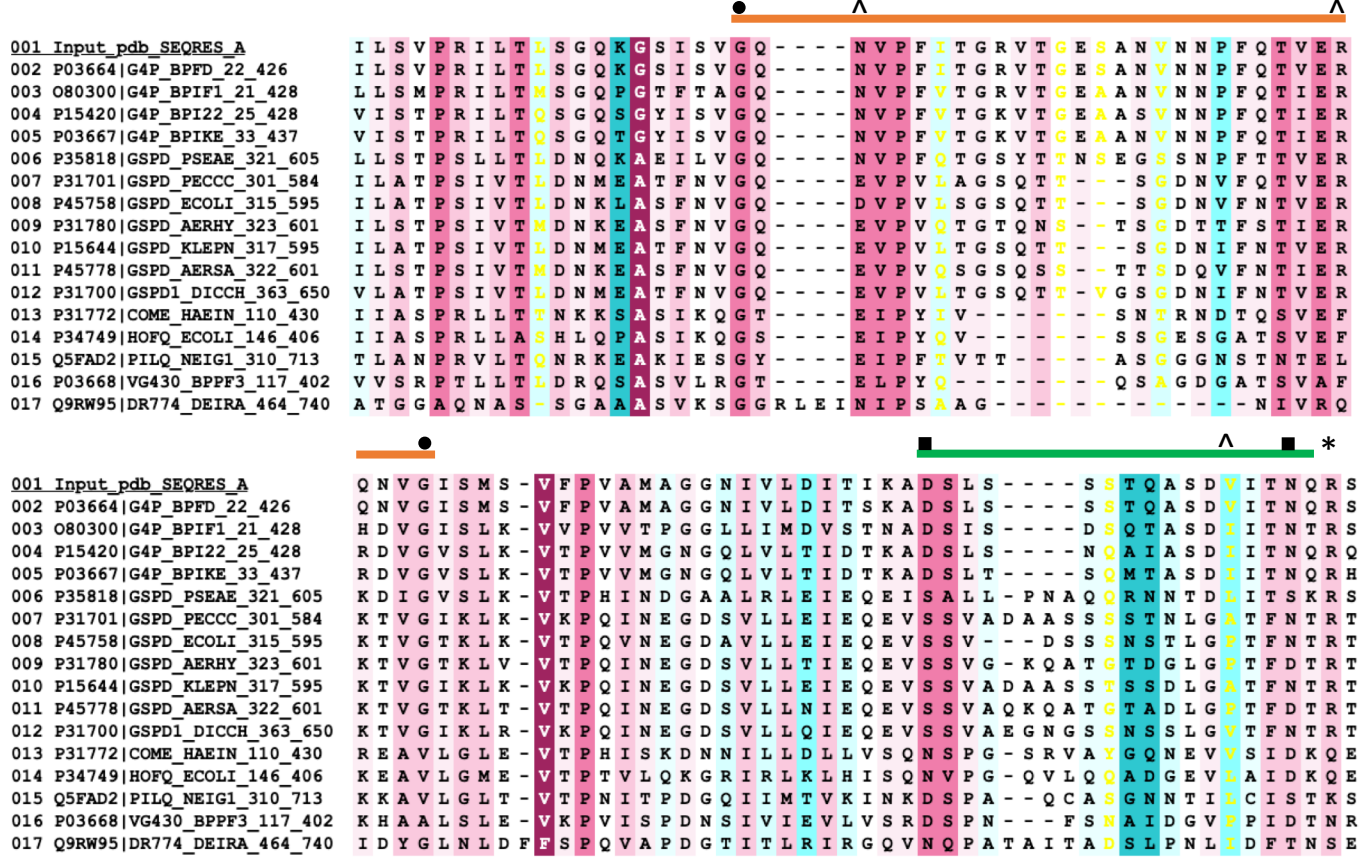
Blue curve = `rlnFourierShellCorrelationMaskedMaps`.

Black curve = `rlnFourierShellCorrelationCorrected`.

b) f1pIV cryoEM map coloured by local resolution (calculated with Resmap)⁶⁰.

c) FSC curve showing the quality of the model to map fit (calculated with Phenix)⁶¹.

Variable Conserved
 1 2 3 4 5 6 7 8 9



Supplementary Figure 3. Sequence alignment of the Gate region of 16 homologues from Swiss-Prot coloured by conservation. Gate 1 is indicated with an orange line and Gate 2 with a green line. ● Hinge residues Gly 267 and Gly 297 in the Gate 1 loop and ■ hinge residues Asp 321 and Asn 335 in the Gate 2 loop. ^ highly conserved Asn 269 and Arg 293 involved in intra-gate hydrogen bonding, and non-conserved Val 332 involved in inter-gate hydrogen bonding via its main chain carbonyl oxygen. * highly conserved Arg 337 found in salt bridge in the interface between the inner and outer β -barrels.

Variable	Conserved								
1	2	3	4	5	6	7	8	9	

```

*
001 Input_pdb_SEQRES_A      I F E V Q Q G D A L D F S F A A G S Q R G T - - - - - V A G G V N T - - - - -
002 P03664|G4P_BPF2_22_426  I F E V Q Q G D A L D F S F A A G S Q R G T - - - - - V A G G V N T - - - - -
003 O80300|G4P_BPIF1_21_428 I F E T T A S D G F D F S F A A G D P S G S P - - - - - V A G G I N T - - - - -
004 P15420|G4P_BPI22_25_428 M F E T S V S N G V D L S F A L A L A S G G K - - - - - V A G G F N T - - - - -
005 P03667|G4P_BPIKE_33_437  M F E T S L V N G V D L S F A A G S A S G D K - - - - - V A G G F N T - - - - -
006 P35818|GSPD_PSEAE_321_605 I V E I S G D I Q D A V G V Q W A I N K G G M - - - - G G T K T N F A N T G L S I G T L L Q S L E S
007 P31701|GSPD_PECCE_301_584 I A E V Q D A D G W N L G V Q W A N K N A G - - - - - V T Q F T N T G L P I T T M M A G A D Q
008 P45758|GSPD_ECOCI_315_595 I V E V Q D G N G L N L G V Q W A N K N V G - - - - - A Q Q F T N T G L P I F N A A Q G V A D
009 P31780|GSPD_AERHY_323_601 I V E I A D G D G L N L G V Q W A N T N G G - - - - - G T Q F T N A G P G I G S V A I A A K D
010 P15644|GSPD_KLEPN_317_595 I A E V Q D A D G L N L G I Q W A N R N A G - - - - - M T Q F T N S G L P I S T A I A G A N Q
011 P45778|GSPD_AERSA_322_601 I V E I A D G D G L N L G V Q W A N T N G G - - - - - G T Q F T D T N L P I G S V A I A A K D
012 P31700|GSPD1_DICCH_363_650 I A E I Q D A D G L N L G I Q W A N K R A G - - - - - M T Q F T N T G I P I S T A M I G T D Q
013 P31772|COME_HAEIN_110_430 I V T I T D E S L K E L G V R W G I F N P T E - - - - - N A R R V A G S L T - - - - - G N S F
014 P34749|HOFQ_ECOCI_146_406 I V T I N E K S L R E L G V K W T L A - - - - - D A Q H A G S V - - - - - G Q V
015 Q5FAD2|PILQ_NEIG1_310_713 I V E A A D G F S R D L G V K F G A T G R K K L K N E T S A F G W G V N S G F G - - - - - G G D K
016 P03668|VG430_BPPF3_117_402 V V E A S V D W S K R L G L N W G G - - - - - A L S L G N W S A V - - - - -
017 Q9RW95|DR774_DEIRA_464_740 I Q E V N E R A L Q S L G L N W R A T F G G F - - - - - N V A V S G G - - - - - T G L - - - - - A A T F

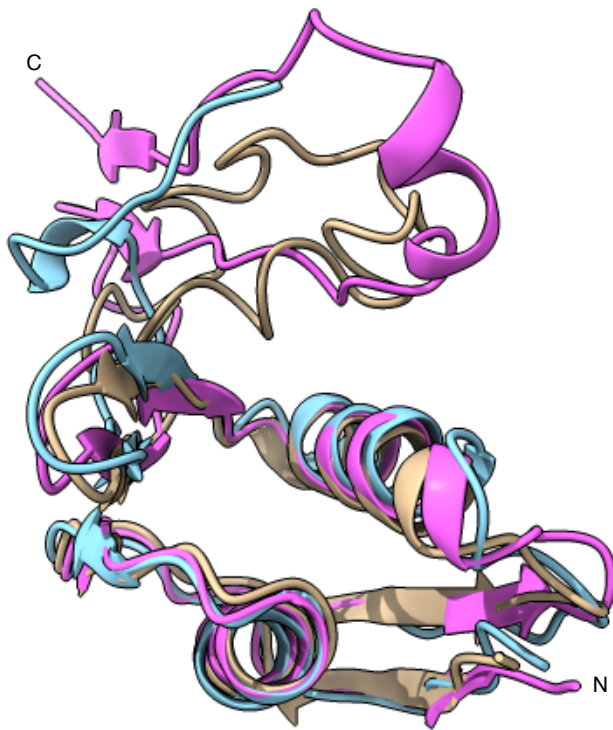
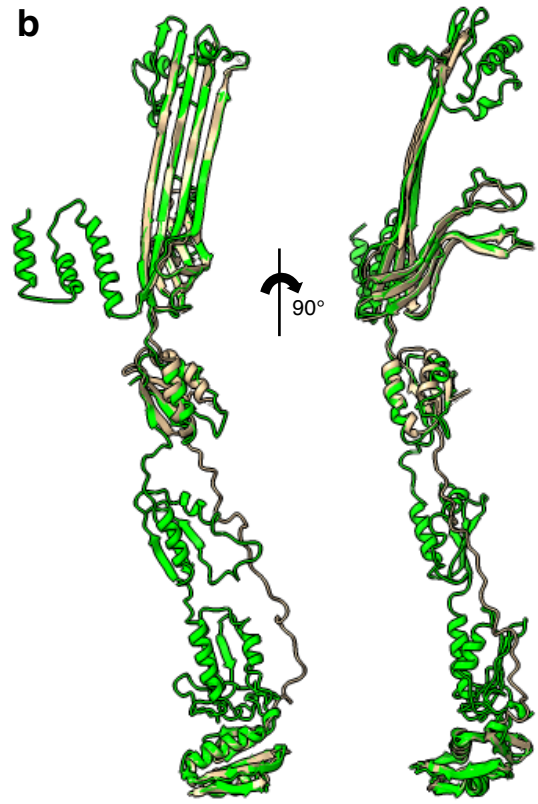
```

```

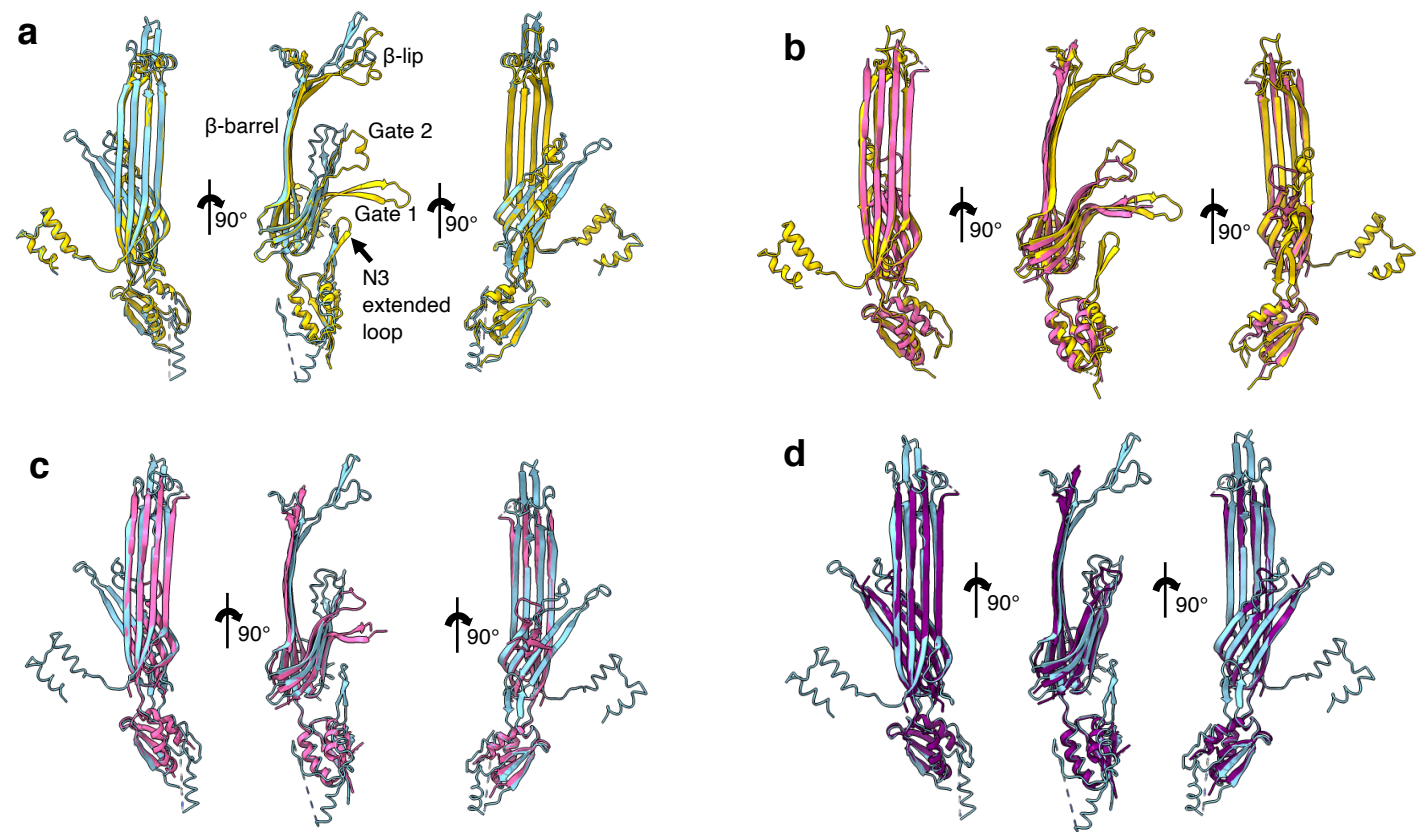
001 Input_pdb_SEQRES_A      - - - - - D R L T S V L S - - - S - - - - - A G G S F G I F N G D V - L G L S V R A L K T N S H S K
002 P03664|G4P_BPF2_22_426  - - - - - D R L T S V L S - - - S - - - - - A G G S F G I F N G D V - L G L S V R A L K T N S H S K
003 O80300|G4P_BPIF1_21_428 - - - - - D R L T S V L S - - - S - - - - - T G G S F G I F N G N I - L G L S L K A L E T S S K S T
004 P15420|G4P_BPI22_25_428 - - - - - S A L G T A L S - - - T - - - - - A G G S F G I F N G N I - L A L S L Q A V Q S D S N S K
005 P03667|G4P_BPIKE_33_437 - - - - - S A L G T A L S - - - T - - - - - A G G S F G I F N G N V - L A L S I Q A V K N D S N S K
006 P35818|GSPD_PSEAE_321_605 N K A P E S I P - - - - - - - - - - D G A I V G I G S S - - F G A L V T A L S A N T K S N
007 P31701|GSPD_PECCE_301_584 F R R D G T L G T A A T - - - T A L - - - G G F N G I A A G F Y Q G N - - W G M L M T A L S S N S K N D
008 P45758|GSPD_ECOCI_315_595 Y K K N G G I T S A N P A W D M F - - - S A Y N G M A A G F F N G D - - W G V L L T A L A S N N K N D
009 P31780|GSPD_AERHY_323_601 Y K D N G T T T G L A - - - K L A - - - E N F N G M A A G F Y Q G N - - W A M L V T A L S T N T K S D
010 P15644|GSPD_KLEPN_317_595 Y N K D G T V S S S L A - - - S A L - - - S F N G I A A G F Y Q G N - - W A M L L T A L S S S T K N D
011 P45778|GSPD_AERSA_322_601 Y N E N G T T T G L A - - - D L A - - - K G F N G M A A G F Y H G N - - W A A L V T A L S T S T K S D
012 P31700|GSPD1_DICCH_363_650 F R S D G T L T T A Y A - - - S A L - - - S N F N G I T A G F Y R G N - - W S M L L T A L S S D G K N D
013 P31772|COME_HAEIN_110_430 E N I A D W L N V N F A - - - T T T P A G S I A L Q V A K I N G R L - L D L E L S A L E R E N N V E
014 P34749|HOFQ_ECOCI_146_406 T T L G S D L S V A T A - - - T T - - - - H V G F N I G R I N G R L - L D L E L S A L E Q Q Q L D
015 Q5FAD2|PILQ_NEIG1_310_713 W E A Q T K I N L P V A - - - A A - - - - A N S I S L V R A I S S G A - - L N L E L S A S E S L S K T K
016 P03668|VG430_BPPF3_117_402 - - - T A G D L S V A A G - - - - - - - - - - S S I G F G F L S N T L S L D G L F T A M E N E G N G R
017 Q9RW95|DR774_DEIRA_464_740 N P T Q S F L G F N I F - - - P T L T A L E T Q G L T R R V Y D G N - - - - - V T M Q S G Q R S L S

```

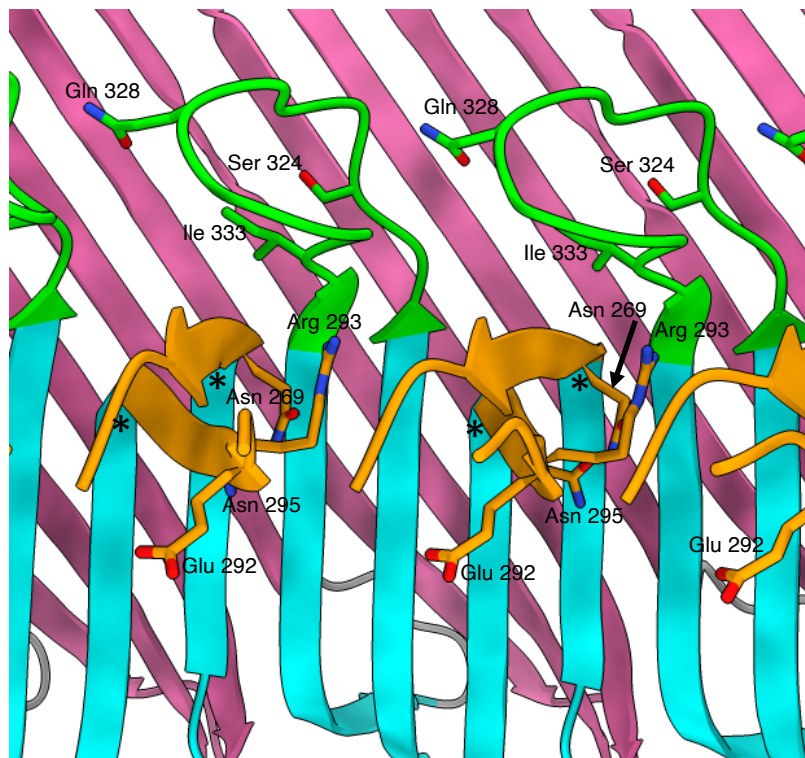
Supplementary Figure 4. Sequence alignment of the β -barrel lip region of 16 homologues from Swiss-Prot coloured by conservation. The cap region is indicated with a blue line. * highly conserved Glu 185 found at top of the interface between the inner and outer β -barrels. Sequences 001-005 and 016 are phage sequences and have 36-37 residues in the β -lip region. The remaining sequences are from bacterial Type II secretion systems and have 51-59 residues in this region.

a**b**

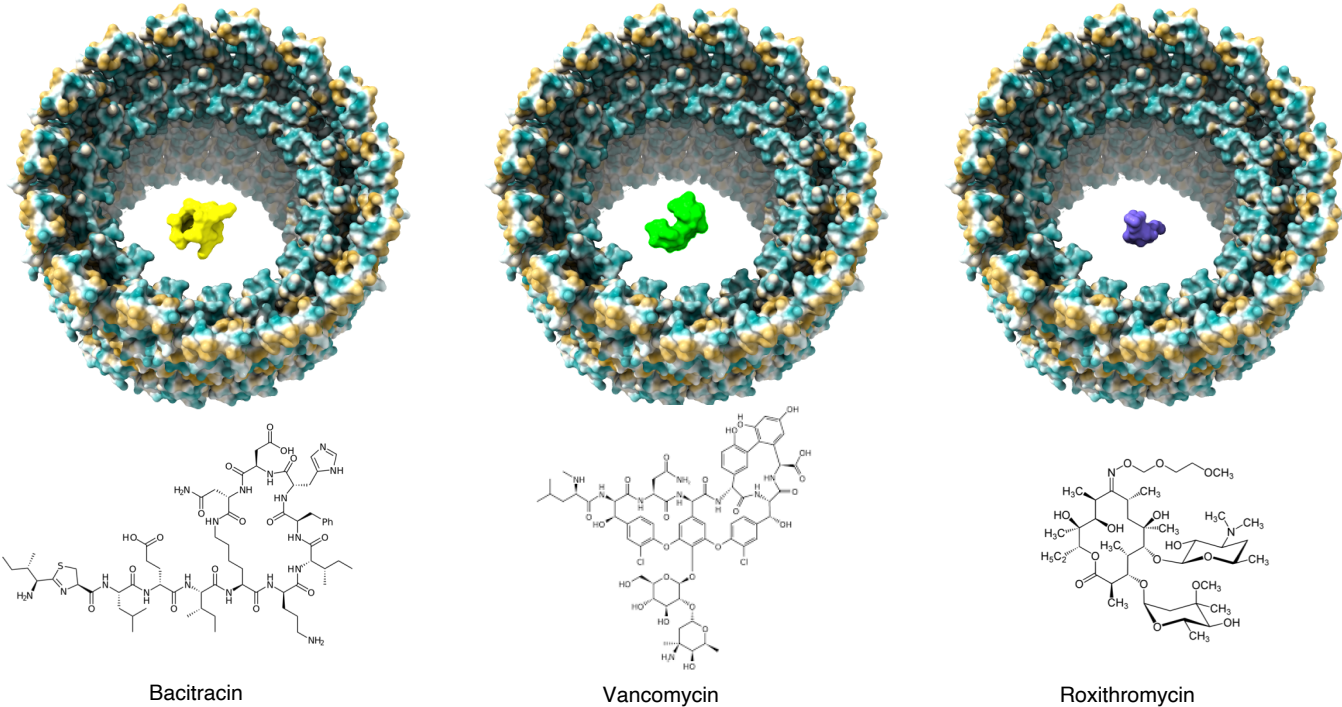
Supplementary Figure 5. Modelling the N0 domain. **a)** Structural superimposition of N0 homology models produced by Swiss-model (blue), I-TASSER (brown) and Robetta (RoseTTAfold algorithm, magenta). The models are in agreement for residues 2-71 (the folded domain) and differ from residues 72-107 (the flexible linker). **b)** Structural superimposition of the PulD secretin from *Klebsiella pneumoniae* (6HCG, green) with flpIV composite model (brown).



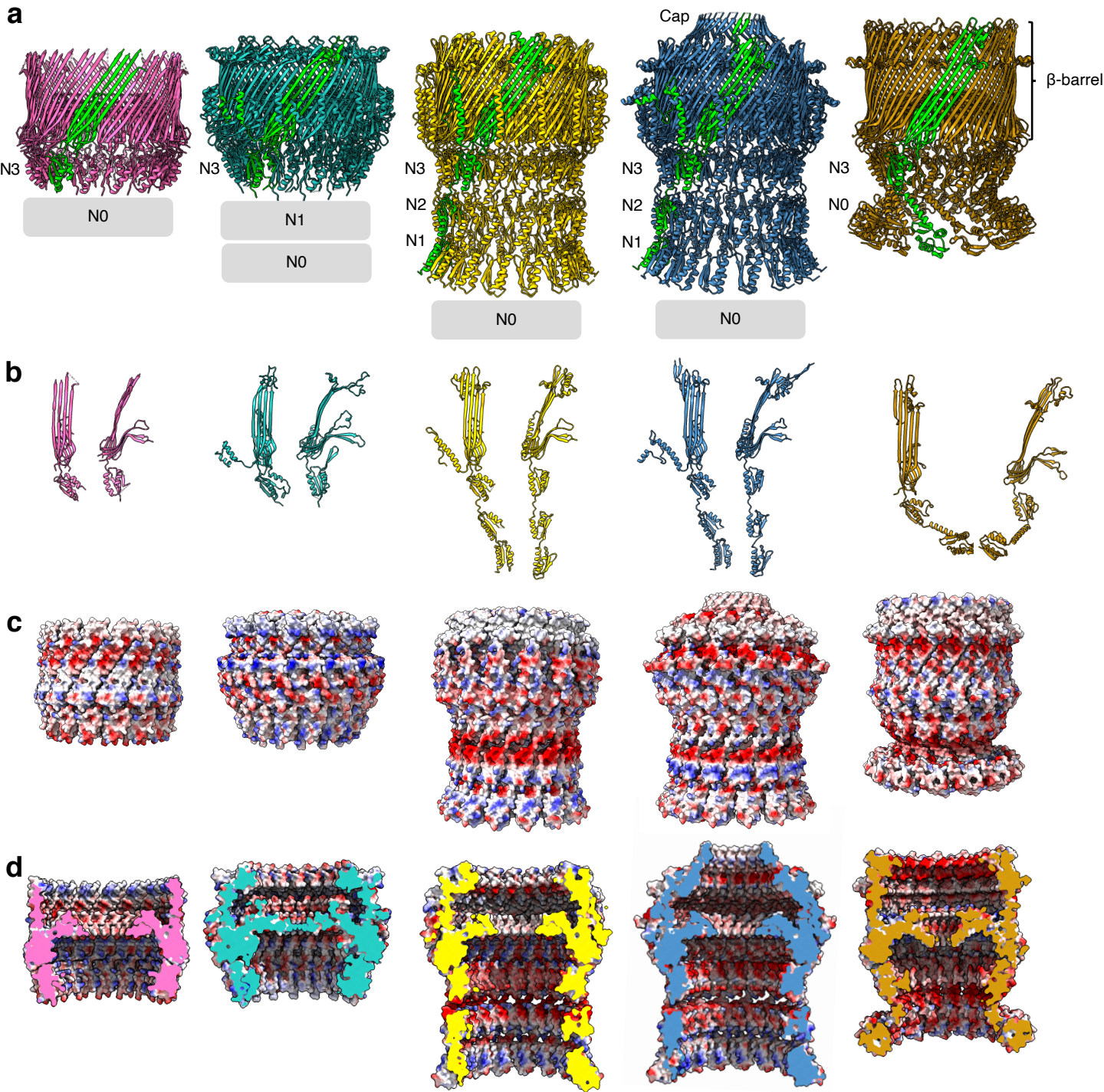
Supplementary Figure 6. Modelling flpIV in the open state. **a)** Structural alignment of open (blue; 6Q15³³) and closed (yellow; 6PEE³³) states of InvG from *Salmonella typhimurium* in front, side and back views from left to right. **b)** Structural alignment of the closed state of InvG (yellow; 6PEE) and flpIV (this study: 7OFH; pink) in front, side and back views from left to right. The average distance between the atoms of the two superimposed proteins was measured using the Root Mean Square Deviation (RMSD), giving a value of 1.051 Å between 94 pruned atom pairs. **c)** Structural alignment of the open state of InvG (blue; 6Q15) and flpIV (this study: 7OFH; pink) in front, side and back views from left to right. **d)** Structural alignment of the open state of InvG (blue, 6Q15) and flpIV modelled in an open form (purple) in front, side and back views from left to right.



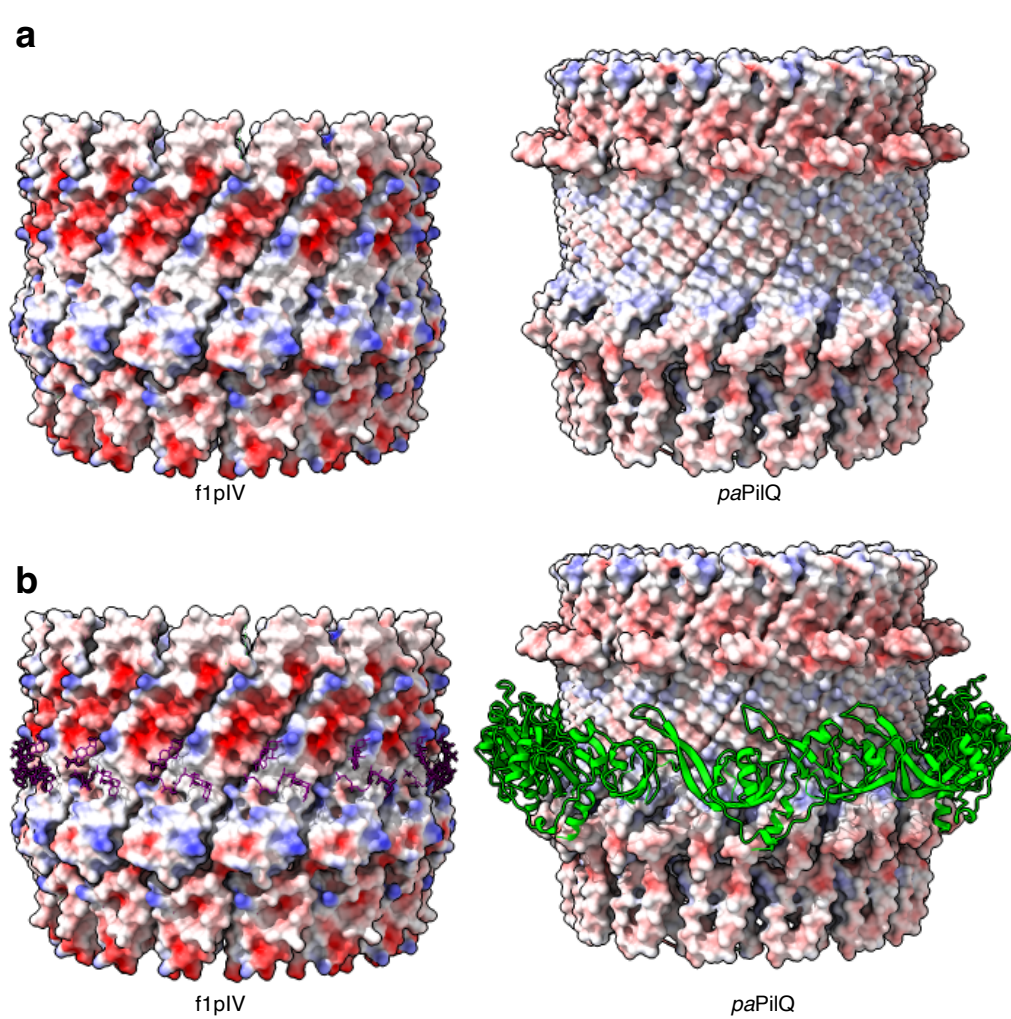
Supplementary Figure 7. f1pIV leaky mutants. An f1pIV 15-mer is shown as a cut-through, viewed from the centre of the pore. Residues Asn 269, Glu 292, Arg 293 and Asn 295 are shown in stick form in the Gate 1 loop (orange), residues Ser 324, Ile 333 and Gln 328 are shown in stick form in the Gate 2 loop (green). Hinge residues Gly 267 and Gly 297 are shown with *. Colouring as per Fig. 2b.



Supplementary Figure 8. Antibiotic uptake through open flpIV. The open flpIV model (coloured by hydrophobicity with the most hydrophobic areas coloured orange, through white, to the most hydrophilic in dark cyan) with bacitracin (yellow, amphipathic), vancomycin (lime green, hydrophilic) and roxithromycin (purple, hydrophobic) shown as surfaces. The chemical structures of each antibiotic are shown below.



Supplementary Figure 9. Structural comparison of flpIV with a selection of different classes of bacterial secretins. Secretins are aligned at the β -barrel domain. flpIV is shown in pink (this study: 7OFH), the Type III secretin InvG from *Salmonella typhimurium* in sea green (6PEE), the Type II secretin GspD from *E. coli* K12 in gold (5WQ7), the Type II secretin GspD from *Vibrio cholerae* in blue (5WQ8) and the Type IV pilus secretin PilQ from *Vibrio cholerae* in orange (6W6M). The secretins are shown in **a**) as multimers (with one monomer coloured lime green). Periplasmic N domains not observed in the map are shown as grey boxes. The corresponding monomers are shown in **b**) in front and side view. **c**) Electrostatic surface potential comparison of multimers and in **d**) cut-through to show the inner surface inside the pore.



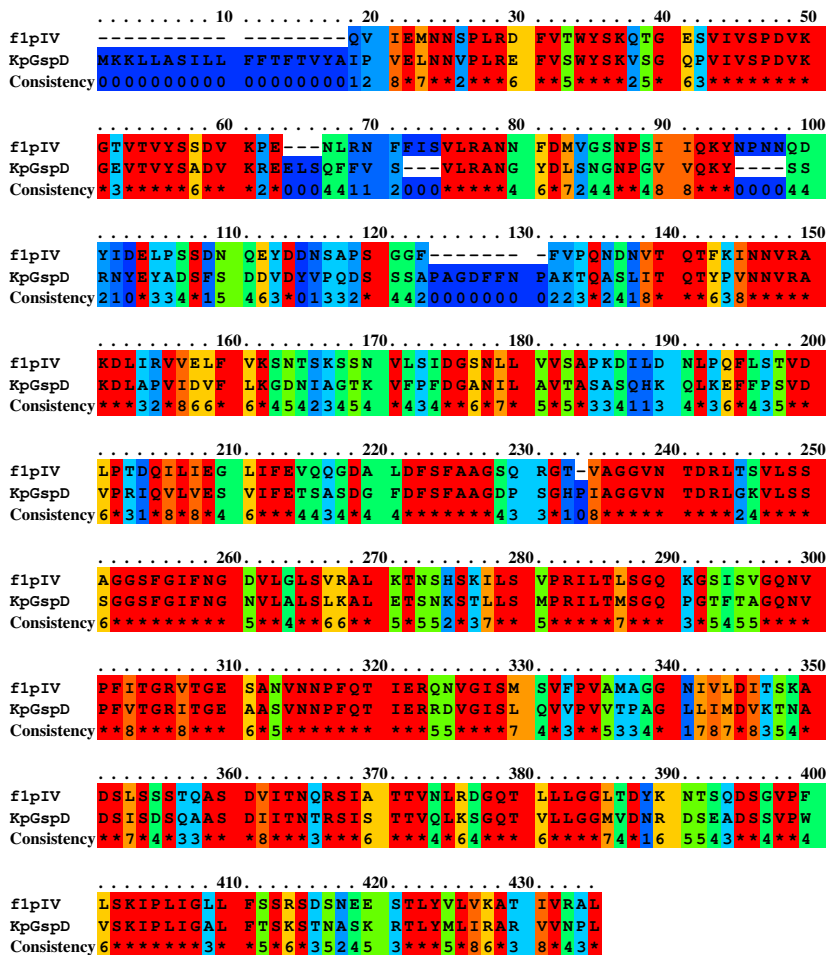
Supplementary Figure 10. Comparison of electrostatic surfaces and pilotin binding. Secretins are aligned at their β -barrel domains. **a)** Electrostatic surface charge representation of f1pIV (this study: 7OFH) and PilQ from *Pseudomonas aeruginosa* (paPilQ) with pilotin removed (6VE2)⁵⁰. **b)** Electrostatic surface charge representation of f1pIV showing CHAPS molecules bound (purple sticks) and paPilQ showing the pilotin TsaP bound (cartoon representation in green).

Results colour-coded for amino acid conservation

The current colourscheme of the alignment is for amino acid conservation.

The conservation scoring is performed by PRALINE. The scoring scheme works from 0 for the least conserved alignment position, up to 10 for the most conserved alignment position. The colour assignments are:

Unconserved 0 1 2 3 4 5 6 7 8 9 10 Conserved



Supplementary Figure 11. Sequence alignment performed with Praline. The closest homologue of f1pIV based on sequence identity is GspD from *Klebsiella pneumoniae*.

Data collection and processing	Dataset 1	Dataset 2
Acceleration voltage (kV)	300	300
Nominal magnification (x)	81k	81k
Pixel size (Å)	1.072	0.536 (super-res)
Frame rate (s ⁻¹)	11.93	11.93
Exposure time (s)	3.52	3.52
Total exposure (e/Å)	42.059	42.059
Particles		
Micrographs used for selection	7037	14,336
Defocus range (μm)	-2.5 to -1.3 (0.2 μm steps)	-2.5 to -1.3 (0.2 μm steps)
Total number of particles	241,591	330,389
In final 3D reconstruction	16104	95575
	Dataset 1 and Dataset 2 combined	
Resolution		
“Gold-standard” at FSC 0.143 (Å)		2.7
Map-sharpening B factor (Å ²)		0
Model refinement		
Model composition	15 identical subunits	
Non-hydrogen atoms, per chain	1742	
Protein residues, per chain	231	
Ligands, per chain	2	
R.M.S. Z scores		
Bond lengths (Å)	0.48	
Bond angles (°)	0.72	
R.M.S.D		
Bond lengths (Å)	0.031	
Bond angles (°)	1.903	
Validation		
Ramachandran angles (%)		
Favoured	88	
Allowed	12	
Outliers	0	
Clashscore	14	
Rotamer outliers (%)	2	
Resolution estimates (Å)		
Model resolution (0/0.143/0.5) - masked	2.5/2.6/2.7	
Model resolution (0/0.143/0.5) - unmasked	2.4/2.5/2.9	

Supplementary Table 1. The statistics of data collection, model reconstruction, refinement and validation.

f1pIV leaky mutation	Location in structure	Leaky to maltopentaose sugars /deoxycholate	Leaky (sensitive) to vancomycin	Leaky (sensitive) to bacitracin
A121V	N3 domain	✓	✗	✗
D123Y	N3 domain	✓	✗	✗
G147V	N3 domain	✓	✗	✗
I183V	Secretin domain	✓	✗	✗
G259S/D	Gate region	✓	✗	✗
S263F	Gate region	✓	✓	✓
G267D	Gate region	✓	✗	✗
N269D	Gate region	✓	✓	✓
V270I	Gate region	✓	✓	✓
P271S	Gate region	✓	✗	✗
I273V	Gate region	✓	✗	✗
G275D	Gate region	✓	✗	✗
R276C	Gate region	✓	✗	✗
V277A	Gate region	✓	✗	✗
G279D	Gate region	✓	✗	✗
S281P	Gate region	✓	✗	✗
A282G	Gate region	✓	✓	✗
N283K	Gate region	✓	✗	✗
V284A	Gate region	✓	✗	✗
F288L	Gate region	✓	✗	✗
E292K	Gate region	✓	✓	✓
R293C	Gate region	✓	✗	✗
N295S	Gate region	✓	✓	✓
V296I	Gate region	✓	✗	✗
G297V	Gate region	✓	✗	✗
S322N	Gate region	✓	✓	✓
S324G	Gate region	✓	✓	✓
S325P	Gate region	✓	✓	✓
S326F	Gate region	✓	✓	✗
T327A	Gate region	✓	✓	✗
Q328G	Gate region	✓	✓	✓
A329T/V	Gate region	✓	✗	✗
S330N	Gate region	✓	✗	✗
D331N	Gate region	✓	✓	✓
I333V	Gate region	✓	✓	✗
T334A	Gate region	✓	✓	✓

Supplementary Table 2. Leaky flpIV mutants. The leaky mutants from Spagnuolo et al²⁴ were plotted onto the flpIV structure shown in Fig. 5a and b.